REPORT DOCUMENTATION PAGE	Form Approved OMB NO. 0704-0188

1. REPORT DATE (DD-MM-YYYY)	2. REPORT TYPE	3. DATES COVERED (From - To)
26-09-2012	Final Report	1-Feb-2011 - 31-Jul-2011

4. TITLE AND SUBTITLE	5a. CONTRACT NUMBER
Peridynamic Applications for Orthotropic Materials	W911NF-11-1-0048
	5b. GRANT NUMBER
	5c. PROGRAM ELEMENT NUMBER 622618
6. AUTHORS Dahsin Liu, Tao Jia	5d. PROJECT NUMBER
	5e. TASK NUMBER
	5f. WORK UNIT NUMBER

7. PERFORMING ORGANIZATION NAMES AND ADDRESSES	8. PERFORMING ORGANIZATION REPORT NUMBER
Michigan State University Hannah Administration Building 426 Auditorium Road, Room 301 East Lansing, MI 48824 -2612	
9. SPONSORING/MONITORING AGENCY NAME(S) AND ADDRESS(ES)	10. SPONSOR/MONITOR'S ACRONYM(S) ARO
U.S. Army Research Office P.O. Box 12211 Research Triangle Park, NC 27709-2211	11. SPONSOR/MONITOR'S REPORT NUMBER(S) 58349-EG.5

12. DISTRIBUTION AVAILIBILITY STATEMENT

Approved for Public Release; Distribution Unlimited

13. SUPPLEMENTARY NOTES

The views, opinions and/or findings contained in this report are those of the author(s) and should not contrued as an official Department of the Army position, policy or decision, unless so designated by other documentation.

14. ABSTRACT

It has been shown that peridynamic simulation of damage process does not require any knowledge of the damage location and orientation prior to the simulation. This is fundamentally different from finite element analysis which requires knowledge of damage location and orientation in advance to impose special finite element mesh, such as initial damage elements and cohesive zone layers [1], for damage simulations. This prerequisite becomes even more challenging when inhomogeneous and anisotropic composite materials are of interest. In addition,

15. SUBJECT TERMS

peridynamic analysis, numerical simulation, orthotropic materials, dynamic testing

16. SECURITY CLASSIFICATION OF:			17. LIMITATION OF ABSTRACT	15. NUMBER OF PAGES	19a. NAME OF RESPONSIBLE PERSON
a. REPORT	b. ABSTRACT	c. THIS PAGE			Dahsin Liu
UU	UU	UU	UU		19b. TELEPHONE NUMBER 517-353-6716

Report Title

Peridynamic Applications for Orthotropic Materials

ABSTRACT

It has been shown that peridynamic simulation of damage process does not require any knowledge of the damage location and orientation prior to the simulation. This is fundamentally different from finite element analysis which requires knowledge of damage location and orientation in advance to impose special finite element mesh, such as initial damage elements and cohesive zone layers [1], for damage simulations. This prerequisite becomes even more challenging when inhomogeneous and anisotropic composite materials are of interest. In addition, peridynamic simulation does not require remeshing at the end of each damage processing step since it is a mesh free method. On the contrary, finite element analysis does. Based on these difference, peridynamics should be more suitable for simulating dynamic damage process in composite materials which have different properties in different locations and different orientations.

Enter List of papers submitted or published that acknowledge ARO support from the start of the project to the date of this printing. List the papers, including journal references, in the following categories:

(a) Papers published in peer-reviewed journals (N/A for none)

Received Paper

TOTAL:

Number of Papers published in peer-reviewed journals:

(b) Papers published in non-peer-reviewed journals (N/A for none)

Received Paper

TOTAL:

Number of Papers published in non peer-reviewed journals:

(c) Presentations

Liu, D., Jia, T. and Li, G., “Numerical Simulation of Q3D Composites for Blast Mitigation,” Abstract, the 10th U.S. National Congress on Computational Mechanics, Columbus, OH, July 15-19, 2009.

Tao Jia and Dahsin Liu, "One-dimensional Peridynamic Analysis and Experimental Validation", the 11th US National Congress on Computational Mechanics, Minneapolis, MN, July 25-28, 2011.

Tao Jia, Development and applications of new peridynamic models, Ph.D Dissertation, Michigan State University, September, 2012.

Number of Presentations: 2.00

Non Peer-Reviewed Conference Proceeding publications (other than abstracts):

Received Paper

TOTAL:

Number of Non Peer-Reviewed Conference Proceeding publications (other than abstracts):

Peer-Reviewed Conference Proceeding publications (other than abstracts):

Received	Paper

TOTAL:

Number of Peer-Reviewed Conference Proceeding publications (other than abstracts):

(d) Manuscripts

Received		Paper
2011/09/19 0ᵢ	4	Tao Jia, Dahisn Liu. Formulation and application of two-dimensional peridynamic beam model, J. Applied Mechanics (to be submitted) (09 2011)
2011/08/28 2ᵢ	3	Dahsin Liu, Tao Jia. Peridynamic analysis and split Hopkinson's pressure bar test, J. Applied Mechanics (to be submitted) (08 2011)

TOTAL: **2**

Number of Manuscripts:

Books

Received	Paper

TOTAL:

Patents Submitted

Patents Awarded

Awards

none

Graduate Students

NAME	PERCENT_SUPPORTED	Discipline
Tao Jia	0.50	
FTE Equivalent:	**0.50**	
Total Number:	**1**	

Names of Post Doctorates

NAME	PERCENT_SUPPORTED
FTE Equivalent:	
Total Number:	

Names of Faculty Supported

NAME	PERCENT_SUPPORTED	National Academy Member
Dahsin Liu	0.20	
FTE Equivalent:	**0.20**	
Total Number:	**1**	

Names of Under Graduate students supported

NAME	PERCENT_SUPPORTED
FTE Equivalent:	
Total Number:	

Student Metrics

This section only applies to graduating undergraduates supported by this agreement in this reporting period

The number of undergraduates funded by this agreement who graduated during this period: 0.00

The number of undergraduates funded by this agreement who graduated during this period with a degree in science, mathematics, engineering, or technology fields:...... 0.00

The number of undergraduates funded by your agreement who graduated during this period and will continue to pursue a graduate or Ph.D. degree in science, mathematics, engineering, or technology fields:...... 0.00

Number of graduating undergraduates who achieved a 3.5 GPA to 4.0 (4.0 max scale):...... 0.00

Number of graduating undergraduates funded by a DoD funded Center of Excellence grant for Education, Research and Engineering:...... 0.00

The number of undergraduates funded by your agreement who graduated during this period and intend to work for the Department of Defense 0.00

The number of undergraduates funded by your agreement who graduated during this period and will receive scholarships or fellowships for further studies in science, mathematics, engineering or technology fields:...... 0.00

Names of Personnel receiving masters degrees

NAME	
Total Number:	

Names of personnel receiving PHDs

NAME	
Tao Jia	
Total Number:	**1**

Names of other research staff

NAME	PERCENT_SUPPORTED
FTE Equivalent:	
Total Number:	

Sub Contractors (DD882)

Inventions (DD882)

Scientific Progress

An orthotropic material model was presented and its applications were studied in this report. A four-parameter peridynamic model for orthotropic materials was proposed to coincide with the four independent material properties required for orthotropic materials. This four-parameter model was different from other models as it had four parameters and was mesh independent. The model was verified by a static tensile test and a vibration excitation of a laminated beam. An SEN (single edge notch) test of a 0° laminated plate was simulated by peridynamics and the computational results matched very well with published experimental results. Fracture initiation and crack path of laminated plates with different fiber orientations were also studied using peridynamics. The mesh-free peridynamic model was convenient and efficient since there was no need to have different meshes for different fiber orientations. Without using special meshes and requiring prior knowledge of fracture paths, a general peridynamic code was able to predict fracture velocity and crack path successfully.

Technology Transfer

Peridynamic Applications for Orthotropic Materials

It has been shown earlier that peridynamic simulation of damage process does not require any knowledge of the damage location and orientation prior to the simulation. This is fundamentally different from finite element analysis which requires knowledge of damage location and orientation in advance to impose special finite element mesh, such as initial damage elements and cohesive zone layers [1], for damage simulations. This prerequisite becomes even more challenging when inhomogeneous and anisotropic composite materials are of interest. In addition, peridynamic simulation does not require remeshing at the end of each damage processing step since it is a mesh free method. On the contrary, finite element analysis does. Based on these difference, peridynamics should be more suitable for simulating dynamic damage process in composite materials which have different properties in different locations and different orientations.

Quite some simulations of composite damage process have been available in the literatures. Dwivedi [1] modeled the propagation of single-edge notch (SEN) in 0° laminated plate using cohesizve zone method. Xu [2] and Hu [3] proposed a two-parameter discrete peridynamic model for composite damage simulations, in which there were two kinds of bonds: fiber bond and matrix bond. Two material properties, a_1 and a_2, were associated with the two types of bonds. Only the bonds along the fiber direction were associated with the material property a_1 while all other bonds with the material property a_2. This model required remeshing for different fiber directions. For example, a 0°-90° grid mesh could only be used for a 0° or 90° laminae. For a $45°$ lamina, a grid mesh consisting of $45°$ and $135°$ was required. The two-parameter model was an aproximation of the four material properties invovled in orthotropic materials. They were mainly associated with two Young's moduli, E_1 and E_2. Its capability of modeling shear behavior is unknown.

In this study, a continuous orthrotropic material model is proposed. It is based on continuous trigonometric functions. With the continuous material property functions, it is not necessary to have bond in fiber direction and therefore, this model is mesh independent.

5.1 Bar model for orthotropic materials

This model is based on the bar model presented in Seciton 4.1. The peridynamic equation of motion [4] in two-dimensional domain can be expressed as

$$\rho \ddot{\boldsymbol{u}} = \int \boldsymbol{f} \, dA \; + \boldsymbol{b} \tag{5.1}$$

where $\boldsymbol{b}$ is external force. The force boundary condition can be included in the external force.

For bar model, the bond function f is

$$f = c \cdot s \tag{5.2}$$

where s is bond stretch. Contrary to the isotropic material model, bond material property c is assumed to be a trigonometric function

$$c = d_1 \cos(\theta - \alpha)^4 + d_2 \cos(\theta - \alpha)^2 + d_3 \tag{5.3}$$

where d_1, d_2 and d_3 are constants and can be identified from composite material properties. θ is bond direction and α is the fiber direction as shown in Fig. 5.1.

Similar to the analysis in the previous chapters, d_1, d_2 and d_3 can be identified from comparing the strain energy densities based on peridynamic analysis and those based on classical mechanics.

Consider a composite plate with the fibers oriented in $\alpha°$ direction and subjected to the following strain field

$$\varepsilon_{xx} = \varepsilon_1 \tag{5.4}$$

$$\varepsilon_{yy} = \varepsilon_2 \tag{5.5}$$

$$\gamma_{xy} = \gamma_{12} \tag{5.6}$$

The three components are independent of one another.

For a bond in θ direction, and connected to a point $\boldsymbol{x}$ in the domain, the bond force should be

$$f = c \cdot (\varepsilon_1 \cos\theta^2 + \varepsilon_2 \sin\theta^2 + \gamma_{12} \sin\theta\cos\theta) \tag{5.7}$$

From Eqn. 4.7, the strain energy in the bond becomes

$$w_b = \frac{c\eta^2}{2\xi} = cs^2\xi/2 \tag{5.8}$$

Substituting Eqn. 5.3 and Eqn. 5.7 into Eqn. 5.8 and integrating w_b over the horizon**,** the strain energy density at the point $\boldsymbol{x}$ should be

$$W = \frac{1}{2}\int w_b\, dA = \frac{1}{2}\int_0^\delta \int_0^{2\pi} \frac{cs^2\xi}{2} \xi\, d\theta d\xi = \delta^3\pi\{16(d_1 + d_2)(\varepsilon_1 - \varepsilon_2)(\varepsilon_1 + \varepsilon_2)\cos 2\alpha + d_1[(\varepsilon_1 - \varepsilon_2)^2 - \gamma_{12}^2]\cos 4\alpha + 2[(3d_1 + 4d_2 + 8d_3)(3\varepsilon_1^2 + 2\varepsilon_1\varepsilon_2 + 3\varepsilon_2^2 + \gamma_{12}^2) + 8(d_1 + d_2)(\varepsilon_1 + \varepsilon_2)\gamma_{12}\sin 2\alpha + d_1(\varepsilon_1 - \varepsilon_2)\gamma_{12}\sin 4\alpha]\}/768 \tag{5.9}$$

Eqn. 5.9 can be simplified to find the coefficient of each independent term, as shown in Table 5.1. The simplification is achieved based on Mathematica [5].

Table 5.1 Simplified Eqn. 5.9 in terms of independent terms

Coefficients	Independent terms
$d_1\delta^3\pi/96$	$\cos\alpha^4\,\varepsilon_1^2$
$d_1\delta^3\pi/96$	$\cos\alpha^4\,\varepsilon_2^2$
$-d_1\delta^3\pi/48$	$\cos\alpha^4\,\varepsilon_1\varepsilon_2$
$-d_1\delta^3\pi/96$	$\cos\alpha^4\,\gamma_{12}^2$
$(3d_1+4d_2)\delta^3\pi/96$	$\cos\alpha^2\,\varepsilon_1^2$
$(-5d_1-4d_2)\delta^3\pi/96$	$\cos\alpha^2\,\varepsilon_2^2$
$d_1\delta^3\pi/48$	$\cos\alpha^2\,\varepsilon_1\varepsilon_2$
$d_1\delta^3\pi/96$	$\cos\alpha^2\,\gamma_{12}^2$
$(3d_1+8d_2+48d_3)\delta^3\pi/768$	ε_1^2
$(35d_1+40d_2+48d_3)\delta^3\pi/768$	ε_2^2
$(5d_1+8d_2+16d_3)\delta^3\pi/384$	$\varepsilon_1\varepsilon_2$
$(5d_1+8d_2+16d_3)\delta^3\pi/768$	γ_{12}^2
$(3d_1+4d_2)\delta^3\pi/96$	$\sin\alpha\cos\alpha\,\gamma_{12}\varepsilon_1$
$(5d_1+4d_2)\delta^3\pi/96$	$\sin\alpha\cos\alpha\,\gamma_{12}\varepsilon_2$
$d_1\delta^3\pi/48$	$\sin\alpha\cos\alpha^3\,\gamma_{12}\varepsilon_1$
$-d_1\delta^3\pi/48$	$\sin\alpha\cos\alpha^3\,\gamma_{12}\varepsilon_2$

On the other hand, from the theory of composite materials [6], the strain energy density under $\varepsilon_{xx} = \varepsilon_1$, $\varepsilon_{yy} = \varepsilon_2$ and $\gamma_{xy} = \gamma_{12}$ is

$$W = \frac{1}{2}\sigma_{xx}\varepsilon_1 + \frac{1}{2}\sigma_{yy}\varepsilon_2 + \frac{1}{2}\sigma_{xy}\gamma_{12} \tag{5.10}$$

The stresses in Eqn. 5.10 can be calculated by

$$\begin{bmatrix}\sigma_{xx}\\ \sigma_{yy}\\ \sigma_{xy}\end{bmatrix} = \begin{bmatrix}Q_{xx} & Q_{xy} & Q_{xs}\\ Q_{xy} & Q_{yy} & Q_{ys}\\ Q_{xs} & Q_{ys} & Q_{ss}\end{bmatrix}\begin{bmatrix}\varepsilon_{xx}\\ \varepsilon_{yy}\\ \gamma_{xy}\end{bmatrix} \tag{5.11}$$

where,

$$Q_{xx} = Q_{11}m^4 + Q_{22}n^4 + 2m^2n^2Q_{12} + 4m^2n^2Q_{66} \tag{5.12}$$

$$Q_{yy} = Q_{11}n^4 + Q_{22}m^4 + 2m^2n^2Q_{12} + 4m^2n^2Q_{66} \tag{5.13}$$

$$Q_{xy} = Q_{11}m^2n^2 + Q_{22}m^2n^2 + (m^4 + n^4)Q_{12} - 4m^2n^2Q_{66} \tag{5.14}$$

$$Q_{xs} = m^3nQ_{11} - mn^3Q_{22} - mn(m^2 - n^2)Q_{12} - 2mn(m^2 - n^2)Q_{66} \tag{5.15}$$

$$Q_{xs} = mn^3Q_{11} - m^3nQ_{22} + mn(m^2 - n^2)Q_{12} + 2mn(m^2 - n^2)Q_{66} \tag{5.16}$$

$$Q_{ss} = m^2n^2Q_{11} + m^2n^2Q_{22} - 2m^2n^2Q_{12} + (m^2 - n^2)^2Q_{66} \tag{5.17}$$

$$m = \cos\alpha \tag{5.18}$$

$$n = \sin\alpha \tag{5.19}$$

$$Q_{11} = \frac{E_1}{1 - v_{12}v_{21}} \tag{5.20}$$

$$Q_{22} = \frac{E_2}{1 - v_{12}v_{21}} \tag{5.21}$$

$$Q_{12} = \frac{E_2v_{12}}{1 - v_{12}v_{21}} \tag{5.22}$$

$$Q_{66} = G_{12} \tag{5.23}$$

E_1, E_1, v_{12} and G_{12} are the four material properties of orthotropic materials. Substituting Eqns. 5.11 - 5.23 into Eqn. 5.10, it yields

$$W = \frac{1}{2(E_1 - E_2 v_{12}^2)}\{(\varepsilon_1^2 E_1^2 + E_1\varepsilon_2^2 E_2 + E_1 G_{12}\gamma_{12}^2 + 2\varepsilon_1 E_1 \varepsilon_2 E_2 v_{12} - E_2 G_{12}\gamma_{12}^2 v_{12}^2)\cos\alpha^4 + 2\gamma_{12}[\varepsilon_2\big(E_1\big(2G_{12} + E_2(-1 + v_{12})\big) - 2E_2 G_{12} v_{12}^2\big) + \varepsilon_1\big(E_1^2 + 2E_2 G_{12} v_{12}^2 - E_1(2G_{12} + E_2 v_{12})\big)]\cos\alpha^3\sin\alpha + [2\varepsilon_1 E_1 \varepsilon_2(E_1 + E_2) + E_1^2\gamma_{12}^2 + 2\varepsilon_1^2 E_1 E_2 v_{12} + 2E_2 G_{12}\gamma_{12}^2 v_{12}^2 + E_1\big(-2G_{12}\gamma_{12}^2 + E_2(\gamma_{12}^2 + 2\varepsilon_2^2 v_{12} - 2\gamma_{12}^2 v_{12})\big)]\cos\alpha^2\sin\alpha^2 + 2\gamma_{12}[E_1^2\varepsilon_2 + 2(-\varepsilon_1 + \varepsilon_2)E_2 G_{12} v_{12}^2 + E_1\left(\varepsilon_1\big(2G_{12} + E_2(-1 + v_{12})\big) - \varepsilon_2(2G_{12} + E_2 v_{12})\right)]\cos\alpha\sin\alpha^3 + [E_1^2\varepsilon_2^2 - E_2 G_{12}\gamma_{12}^2 v_{12}^2 + E_1(\varepsilon_1^2 E_2 + G_{12}\gamma_{12}^2 + 2\varepsilon_1\varepsilon_2 E_2 v_{12})]\sin\alpha^4 + (\varepsilon_1 - \varepsilon_2)^2 G_{12}(E_1 - E_2 v_{12}^2)\sin 2\alpha^2\} \tag{5.24}$$

After simplification processes, the coeffiencet of each independent terms can be found. They are listed in Table 5.2.

Table 5.2 Simplified Eqn. 5.12 in terms of independent terms

Coefficients	Independent terms
$\frac{E_1^2 + 4E_2 G_{12} v_{12}^2 + E_1(E_2 - 4G_{12} - 2E_2 v_{12})}{2(E_1 - E_2 v_{12}^2)}$	$\cos\alpha^4\,\varepsilon_1^2$
$\frac{E_1^2 + 4E_2 G_{12} v_{12}^2 + E_1(E_2 - 4G_{12} - 2E_2 v_{12})}{2(E_1 - E_2 v_{12}^2)}$	$\cos\alpha^4\,\varepsilon_2^2$
$-\frac{E_1^2 + 4E_2 G_{12} v_{12}^2 + E_1(E_2 - 4G_{12} - 2E_2 v_{12})}{(E_1 - E_2 v_{12}^2)}$	$\cos\alpha^4\,\varepsilon_1\varepsilon_2$

$-\frac{E_1^2+4E_2G_{12}v_{12}^2+E_1(E_2-4G_{12}-2E_2v_{12})}{2(E_1-E_2v_{12}^2)}$	$\cos\alpha^4\,\gamma_{12}^2$
$\frac{E_1(2G_{12}+E_2(-1+v_{12}))-2E_2G_{12}v_{12}^2}{E_1-E_2v_{12}^2}$	$\cos\alpha^2\,\varepsilon_1^2$
$\frac{-E_1^2+2E_1G_{12}+E_1E_2v_{12}-2E_2G_{12}v_{12}^2}{E_1-E_2v_{12}^2}$	$\cos\alpha^2\,\varepsilon_2^2$
$\frac{E_1^2+4E_2G_{12}v_{12}^2+E_1(E_2-4G_{12}-2E_2v_{12})}{E_1-E_2v_{12}^2}$	$\cos\alpha^2\,\varepsilon_1\varepsilon_2$
$\frac{E_1^2+4E_2G_{12}v_{12}^2+E_1(E_2-4G_{12}-2E_2v_{12})}{2(E_1-E_2v_{12}^2)}$	$\cos\alpha^2\,\gamma_{12}^2$
$\frac{E_1E_2}{2(E_1-E_2v_{12}^2)}$	ε_1^2
$\frac{E_1^2}{2(E_1-E_2v_{12}^2)}$	ε_2^2
$\frac{E_1E_2v_{12}}{E_1-E_2v_{12}^2}$	$\varepsilon_1\varepsilon_2$
$\frac{E_1G_{12}-E_2G_{12}v_{12}^2}{2(E_1-E_2v_{12}^2)}$	γ_{12}^2
$\frac{E_1(2G_{12}+E_2(-1+v_{12}))-2E_2G_{12}v_{12}^2}{E_1-E_2v_{12}^2}$	$\sin\alpha\cos\alpha\,\gamma_{12}\varepsilon_1$
$\frac{E_1^2+2E_2G_{12}v_{12}^2+E_1(-2G_{12}-E_2v_{12})}{E_1-E_2v_{12}^2}$	$\sin\alpha\cos\alpha\,\gamma_{12}\varepsilon_2$
$\frac{E_1^2+4E_2G_{12}v_{12}^2+E_1(E_2-4G_{12}-2E_2v_{12})}{(E_1-E_2v_{12}^2)}$	$\sin\alpha\cos\alpha^3\,\gamma_{12}\varepsilon_1$
$-\frac{E_1^2+4E_2G_{12}v_{12}^2+E_1(E_2-4G_{12}-2E_2v_{12})}{(E_1-E_2v_{12}^2)}$	$\sin\alpha\cos\alpha^3\,\gamma_{12}\varepsilon_2$

Eqn. 5.9 should be equal to Eqn. 5.24. Hence, it is possible to set the coefficients of identical

terms equal to each other and identify d_1, d_2 and d_3.

$$d_1 = \frac{24}{\delta^3 E_1 \pi}\left(E_1^2 + E_1E_2 - 12E_1G_{12} + \frac{E_1\sqrt{E_1E_2+4G_{12}^2}}{\sqrt{\frac{E_2}{E_1}}} + \sqrt{E_1E_2}\sqrt{E_1E_2 + 4G_{12}^2}\right) \tag{5.25}$$

$$d_2 = \frac{6}{\delta^3 E_1 \pi}\left(-3E_1^2 - 5E_1E_2 + 48E_1G_{12} - \frac{3E_1\sqrt{E_1E_2+4G_{12}^2}}{\sqrt{\frac{E_2}{E_1}}} - 5\sqrt{E_1E_2}\sqrt{E_1E_2 + 4G_{12}^2}\right) \tag{5.26}$$

$$d_3 = \frac{3}{2\delta^3 E_1 \pi}(E_1^2 + 5E_1E_2 - 20E_1G_{12} + \frac{E_1\sqrt{E_1E_2+4G_{12}^2}}{\sqrt{E_2/E_1}} + 5\sqrt{E_1E_2}\sqrt{E_1E_2 + 4G_{12}^2} \tag{5.27}$$

$$v_{12} = \frac{-E_1E_2+\sqrt{E_1E_2}\sqrt{E_1E_2+4G_{12}^2}}{2E_2G_{12}} \tag{5.28}$$

The composite model has three parameters and it can model shearing deformation. The bond stiffness is a continuous function so the stiffness at any direction can be calculated. It can be found that the bond becomes stronger as the angle between the bond and the fiber becomes smaller. Similar to the bar model in Section 4.1, the Poisson's ratio of this model is fixed and is related to the remaining three independent material properties. For example, the Poisson's ratio of Kevlar/Epoxy is 0.34 while the Poisson's ratio calculated from this model is 0.39.

5.2 Beam model for orthotropic materials

To accomondate the four material properties of orthotropic materials, a beam model based on Section 4.2 is proposed here.

From the composite theory, there are four independent material properties, E_1, E_2, v_{12} and G_{12}. The composite stiffness varies with fiber orientation. Bond functions are

$$f'_x = \frac{c_1(u'_2 - u'_1)}{r} \tag{5.29}$$

$$f'_y = \frac{c_2(v'_2 - v'_1)}{r^3} \tag{5.30}$$

They are identifcal to Eqn. 4.23 and Eqn. 4.24. However, c_1 and c_2 for a bond in θ direction will be dependent on fiber orientations as follows,

$$c_1 = d_1 \cos(\theta - \alpha)^4 + d_2 \cos(\theta - \alpha)^2 + d_3 \tag{5.31}$$

$$c_2 = d_4 \tag{5.32}$$

where α is the orientation of the fiber, as shown in Fig. 5.3. The coefficients d_1, d_2, d_3 and $d_4$are four independent material properties. They are related to the four material properties defined in the composite theory.

Consider a composite plate with fiber in α direction and subject to the following strain field

$$\varepsilon_{xx} = \varepsilon_1 \tag{5.33}$$

$$\varepsilon_{yy} = \varepsilon_2 \tag{5.34}$$

$$\gamma_{xy} = \gamma_{12} \tag{5.35}$$

The three strains are independent from each other.

Similar to Eqn. 4.29, the strain energy in one bond becomes

$$w_b = \frac{c_1(\varepsilon_1 r \cos\theta^2 + \varepsilon_2 r \sin\theta^2)^2}{2r} + \frac{c_2(-\varepsilon_1 r \cos\theta \sin\theta + \varepsilon_2 r \cos\theta \sin\theta)^2}{2r^3} \tag{5.36}$$

Integrate Eqn. 5.36 to find the strain energy density for a point

$W = \frac{1}{2}\int w_b\, dA = \frac{1}{2}\int_0^\delta \int_0^{2\pi} w_b\, r d\theta dr = \frac{1}{768}\pi\delta\{16(d_1 + d_2)\delta^2(\varepsilon_1^2 - \varepsilon_2^2)\cos 2\alpha +$

$$d_1\delta^2(\varepsilon_1^2 - 2\varepsilon_1\varepsilon_2 + \varepsilon_2^2 - \gamma_{12}^2)\cos 4\alpha + 2[24d_4(\varepsilon_1 - \varepsilon_2)^2 + 9d_1\delta^2\varepsilon_1^2 + 12d_2\delta^2\varepsilon_1^2 +$$

$$24d_3\delta^2\varepsilon_1^2 + 6d_1\delta^2\varepsilon_1\varepsilon_2 + 8d_2\delta^2\varepsilon_1\varepsilon_2 + 16d_3\delta^2\varepsilon_1\varepsilon_2 + 9d_1\delta^2\varepsilon_2^2 + 12d_2\delta^2\varepsilon_2^2 + 24d_3\delta^2\varepsilon_2^2 +$$

$$24d_4\gamma_{12}^2 + 3d_1\delta^2\gamma_{12}^2 + 4d_2\delta^2\gamma_{12}^2 + 8d_3\delta^2\gamma_{12}^2 + 8(d_1 + d_2)\delta^2(\varepsilon_1 + \varepsilon_2)\gamma_{12}\sin 2\alpha +$$

$$d_1\delta^2(\varepsilon_1 - \varepsilon_2)\gamma_{12}\sin 4\alpha]\} \tag{5.37}$$

The Strain energy density based on the composite theory is the same as Eqn. 5.24. Similar to Section 5.1, by setting Eqn. 5.24 equal to Eqn. 5.37 and comparing the coefficients of the independent terms, the following equations are obtained

$$d_1 = \frac{48(E_1^2+E_1E_2-4E_1G_{12}-2E_1E_2v_{12}+4E_2G_{12}v_{12}^2)}{\pi(E_1-E_2v_{12}^2)\delta^3} \tag{5.38}$$

$$d_2 = -\frac{12(3E_1^2+5E_1E_2-16E_1G_{12}-8E_1E_2v_{12}+16E_2G_{12}v_{12}^2)}{\pi(E_1-E_2v_{12}^2)\delta^3} \tag{5.39}$$

$$d_3 = \frac{3(E_1^2+5E_1E_2-8E_1G_{12}-2E_1E_2v_{12}+8E_2G_{12}v_{12}^2)}{\pi(E_1-E_2v_{12}^2)\delta^3} \tag{5.40}$$

$$d_4 = -\frac{4(-E_1G_{12}+E_1E_2v_{12}+E_2G_{12}v_{12}^2)}{\pi(E_1-E_2v_{12}^2)\delta} \tag{5.41}$$

5.3 Calculation of stresses from peridynamics

Similar to Section 4.2, stresses can be defined and calculated from peridyamics. They can be used for some special comparison but not necessary in peridynamic simulations.

Consider a case with $\varepsilon_{xx} = \varepsilon_1$ and $\varepsilon_{yy} = \varepsilon_2$. The stress σ_{xx} can be calcualted by using Eqn. 4.39 and is given below

$$\sigma_{xx} = \int_0^\delta \int_t^\delta \int_{-\cos^{-1}\frac{t}{r}}^{\cos^{-1}\frac{t}{r}} (fx' \cdot \cos\theta - fy' \cdot \sin\theta) r\, d\theta dr dt = \frac{1}{384}\pi\delta\{48d_4(\varepsilon_1 - \varepsilon_2) +$$

$$2(3d_1+4d_2+8d_3)(3\varepsilon_1+\varepsilon_2)\delta^2+\delta^2[16\varepsilon_1\cos 2\alpha\,(d_1+d_2)+d_1(\varepsilon_1-\varepsilon_2)\cos 4\alpha]\} \quad (5.42)$$

Substituting Eqns. 5.38 - 5.41 into Eqn. 5.42, it yields

$$\sigma_{xx}=$$

$$\frac{1}{8(E_1-E_2v_{12}^2)}\{3\varepsilon_1E_1^2+\varepsilon_2E_1^2+3\varepsilon_1E_1E_2+\varepsilon_2E_1E_2+4\varepsilon_1E_1G_{12}-4\varepsilon_2E_1G_{12}+2\varepsilon_1E_1E_2v_{12}+$$

$$6\varepsilon_2E_1E_2v_{12}-4\varepsilon_1E_2G_{12}v_{12}^2+4\varepsilon_2E_2G_{12}v_{12}^2+4\varepsilon_1E_1(E_1-E_2)\cos 2\alpha+(\varepsilon_1-\varepsilon_2)\big(E_1^2+$$

$$4E_2G_{12}v_{12}^2+E_1(E_2-4G_{12}-2E_2v_{12})\big)\cos 4\alpha\} \quad (5.43)$$

While from the composite theory, σ_{xx} can be expressed as

$$\sigma_{xx}=Q_{xx}\varepsilon_1+Q_{xy}\varepsilon_2=\frac{1}{(E_1-E_2v_{12}^2)}\{E_1(\varepsilon_1E_1+\varepsilon_2E_2v_{12})\cos a^4+[E_1^2\varepsilon_2+4(-\varepsilon_1+$$

$$\varepsilon_2)E_2G_{12}v_{12}^2+E_1(\varepsilon_2E_2+4\varepsilon_1G_{12}-4\varepsilon_2G_{12}+2\varepsilon_1E_2v_{12})]\cos a^2\sin a^2+E_1E_2(\varepsilon_1+$$

$$\varepsilon_2v_{12})\sin a^4\} \quad (5.44)$$

With further simplification, it can be found that Eqn. 5.43 is identical to Eqn. 5.44.

5.4 Laminated plate under static loading

In this section, it is to verify the proposed peridynamic model with an anlytical solution. A simple tensile test is performed on a laminated plate. The peridynamic results will be compared with the results obtained from the composite theory.

Consider a $100\ mm\times 100\ mm$ laminated plate with fibers in α direction as shown in Fig. 5.4. A tensile pressure of $10\ MPa$ is applied at the bottom and the top of the plate. The plate is made of

E-Glass/Epoxy and the material properties are shonw in Table 5.3.

Table 5.3 Material propteties of E-Glass/Epoxy

Longitudinal Young's modulus, E_1	$41\ GPa$
Transverse Young's modulus, E_2	$10.4\ GPa$
Poisson's ratio, v_{12}	0.28
Shear modulus, G_{12}	$4.3\ GPa$
Mass density, ρ	$1970\ kg/m^3$

Based on the composite theory [6], the components of the complicance matrix are

$$S_{11} = 1/E_1 \tag{5.45}$$

$$S_{22} = 1/E_2 \tag{5.46}$$

$$S_{12} = -v_{12}/E_1 \tag{5.47}$$

$$S_{66} = 1/G_{12} \tag{5.48}$$

Strains from the composite theory can be calcuated as follows

$$\begin{bmatrix} \varepsilon_{xx} \\ \varepsilon_{yy} \\ \gamma_{xy} \end{bmatrix} = \begin{bmatrix} S_{xx} & S_{xy} & S_{xs} \\ S_{xy} & S_{yy} & S_{ys} \\ S_{xs} & S_{ys} & S_{ss} \end{bmatrix} \begin{bmatrix} \sigma_{xx} \\ \sigma_{yy} \\ \sigma_{xy} \end{bmatrix} \tag{5.49}$$

The transformed compliance matrix is caculated as

$$\begin{bmatrix} S_{xx} & S_{xy} & S_{xs} \\ S_{xy} & S_{yy} & S_{ys} \\ \frac{1}{2}S_{xs} & \frac{1}{2}S_{ys} & \frac{1}{2}S_{ss} \end{bmatrix} = T^{-1} \begin{bmatrix} S_{11} & S_{12} & 0 \\ S_{12} & S_{22} & 0 \\ 0 & 0 & \frac{1}{2}S_{66} \end{bmatrix} T \tag{5.50}$$

where

$$T = \begin{bmatrix} m^2 & n^2 & 2mn \\ n^2 & m^2 & -2mn \\ -mn & mn & m^2 - n^2 \end{bmatrix} \quad (5.51)$$

and $m = \cos\alpha$ and $n = \sin\alpha$.

From Eqn. 5.49, the displacement field can be obtained from the composite theory. Displacements from peridynamics are compared with those from the composite theory in Fig. 5.5-Fig. 5.10 with $\alpha = 0°, 45°$ and $60°$. As can be seen, the results from peridynamics and those from composite theory are identical to each other.

5.5 Free vibration of a laminated beam

The free vibration of a laminated beam is investigated in this section by the Classical Laminated Beam Theory and the solution will be used to verify that obtained from peridynamic model.

Consider a simply supported beam as shown Fig. 5.11. The length of the beam is $L = a \cdot h$ and the thickness of the beam is $h = 10\ mm$, where a is the aspect ratio of the beam. The beam is made of Kevlar/Epoxy with fibers oriented in x direction. The material properties are shonw in Table 5.4.

Table 5.4 Material propteties of Kevlar/Epoxy

Longitudinal Young's modulus, E_1	80 GPa
Transverse Young's modulus, E_2	5.5 GPa
Poisson's ratio, v_{12}	0.34
Shear modulus, G_{12}	2.2 GPa

Mass density, ρ	$1380\ kg/m^3$

From [7], the governing equations of the beam are

$$A_{11}\frac{d^2u^\circ}{dx^2} - B_{11}\frac{d^3w}{dx^3} - \rho\omega^2 u^\circ = 0 \tag{5.52}$$

$$D_{11}\frac{d^4w}{dx^4} - B_{11}\frac{d^3u^\circ}{dx^3} - \rho\omega^2 w = 0 \tag{5.53}$$

where

$$A_{11} = \int_{-h/2}^{h/2} Q_{11}\, dz = Q_{11}h \tag{5.54}$$

$$B_{11} = \int_{-h/2}^{h/2} Q_{11}\, zdz = 0 \tag{5.55}$$

$$D_{11} = \int_{-h/2}^{h/2} Q_{11}z^2\, dz = Q_{11}h^3/12 \tag{5.56}$$

A solution satisfying the governing equations is

$$u_0 = U\cos px \tag{5.57}$$

$$w = W\sin px \tag{5.58}$$

Eqn. 5.57 and Eqn. 5.58 satisfy the simply supported boundary conditions automatically. Substituting Eqn. 5.57 and Eqn. 5.58 into Eqn. 5.52 and Eqn. 5.53, it yields

$$-A_{11}p^2U - \rho\omega^2U = 0 \tag{5.59}$$

$$D_{11}p^4W - \rho\omega^2W = 0 \tag{5.60}$$

Solving Eqn. 5.59 and Eqn. 5.60, it can be concluded that

$$\omega^2 = \frac{Q_{11}p^4h^3}{12\rho} \tag{5.61}$$

$$U = 0 \quad (5.62)$$

If the initial condition of the beam is

$$w(t = 0) = 1 \times 10^{-5} \sin \frac{\pi}{L} x \quad (5.63)$$

then

$$W = 1 \times 10^{-5} \quad (5.64)$$

$$p = \frac{\pi}{L} \quad (5.65)$$

The solution of the problem should have the following forms

$$w'(x, t) = W \sin px \cos \omega t \quad (5.66)$$

$$u'(x, z, t) = -zpW \cos px \cos \omega t \quad (5.67)$$

where W, p and ω can be found from Eqn. 5.64, Eqn. 5.65 and Eqn. 5.61, respectively.

The same problem can be simulated by peridynamics. The displacement history of point A and point B (Fig. 5.11) are recorded. Fig. 5.12 compares the peridynamic results with those from the composite beam theory for the aspect ratio $a = 5$. Fig. 5.13 compares the peridynamic results with those from the composite beam theory for the aspect ratio $a = 20$. Results from the two methods show good match in vertical displacement w of point B. For horizontal displacement u of point A, peridynamic result is almost the same as the beam theory result when the aspect ratio $a = 20$. However, there is difference between the peridynamic result and the beam theory result when the aspect ratio $a = 5$. This is because the beam theory assumes no variation of vertical displacement when the beam is slender. With a small aspect ratio, such as $a = 5$, this variation is not neglible and the beam theory does not provide a good approximation.

5.6 Comparisons of crack propagation velocity with experiments

Experimental studies on dynamic crack propagation in fiber-reinforced composite materials have been conducted by Zheng[9], Rosakis[8], Stout[10] and Coker[11,12]. It has been shown that a weak fracture plane usually occurs between fiber and matrix in unidirectional fiber-reinforced composites. Due to material anisotropy, the wave speed along the fiber direction is very different from that along the perpendicular direction. Dynamic crack propagation has been commonly investigated by finite element method. A limited number of computational studies have been reported by Huang [13], Hwang [14], Kumar [15], Stout [10], Lo [16], Sun [17] and Pandey[18]. The limit of computational works is likely due to the requirement of remeshing and the complexity of handling elements once crack starts. In this section, dynamic crack propagation in a unidirectional graphite/epoxy composite is studied with the use of peridynamics. The computational results are validated by the experimental results given in refefrence [8].

Consider a $76\ mm \times 152\ mm$ unidirectional graphite/epoxy fiber-reinforced composite plates under three-point bending [8] as shown in Fig. 5.14. The fiber is in $0°$ direction. The material properties are shown in Table 5.5 [8, 22]. There is a notch with a length of $15.2\ mm$, i.e. 20% of the plate width, at the left boundary of the plate. This crack length is used because it was used in the past to produce reliable results in dynamic fracture experiements [19]. To minimize residual stresses due to machining, a low-speed diamond saw was used to produce the initial notch with a widtch of approximately $1.5\ mm$.

Table 5.5 Material propteties of graphite/epoxy

Longitudinal Young's modulus, E_1	$150\ GPa$
Transverse Young's modulus, E_2	$11.6\ GPa$
Poisson's ratio, v_{12}	0.36
Shear modulus, G_{12}	$3.5\ GPa$
Mode I intralaminar fracture energy for longitudinal loading, G_{10}	$77.9\ J/m^2$
Mode I intralaminar fracture energy for transver loading, G_{20}	$5\ J/m^2$
Mass density, ρ	$1590\ kg/m^3$

A drop-weight tower is used to introduce impact on the opposite side of the notch with an impacting speed of $v_0 = 4\ m/s$. After the impact, stress waves propagate to the interior of the plate and then reflects from the boundaries. Because of the anisotropy of the material, stress waves travel in different directions at different velocities. Experiments show that the crack starts to propagate at about $25\mu s$ after the impact so the effects of dispersion are not very important since the applied stress pulse is very long (about $120\ \mu s$) compared with the time of crack initiation. Therefore, loading is continuously applied throughout the entire event.

The real-time visualization of dynamic fracture is produced by an optical method of coherent gradient sensing (CGS) in reflection [20, 21]. Imaging is performed with a rotating-mirror high-speed camera. Details of the CGS system can be found in [8, 20, 21].

Fig. 5.15 shows the crack propgation velocity from the peridynamic simulation. The initial ime $t = 0$ is used to denote the beginning of the crack propagation. For negtive time, $v = 0\ m/s$. The crack starts from about $700\ m/s$ and accelerates to $900\ m/s$ within about $10\ \mu s$. It then decelerates to less than $500\ m/s$ in $40\ \mu s$ after the initiation. This deceleration is believed to be due to the fact that the growing crack tip enters a region of high compressive stress zone as it appoaches the loading area. The peridynamic computational results are compared with the experimental results from Ref. [8]. As shown in Fig. 5.15, they agree each other reasonably well.

5.7 Dynamic fracture mode in unidirectional composites

In order to investigate the behavior of cracks, Wu [24] conducted experiments with unidirectional, fiberglass-reinforced Scotch composites with a centered precrack in the direction of fibers. The composites were loaded with tension, pure shear and combined tension and shear. In all three cases, it was observed that the crack propagated in the same direction as the fiber direction. Finite element analysis were also used to study the damage path and failure initiation of pre-notched composites by Boger [25] and Satyanarayana [26]. They prediected damge in composite plates notched in the center for different layups under tension. Both experimental results and simulation results showed that the crack path and failure initiation depends on fiber orientation.

In this section, the crack propagation path and dynamic fracture mode of unidirectional fiber-reinforced composites are studied using the proposed peridynamic model. The qualitive comparison of the peridynamic results with those from experiments are of interest.

Consider the compact tension test on a $100\ mm \times 200\ mm$ carbon/epoxy unidirectional composite plate with a $20\ mm$ pre-notch at the center as shown in Fig. 5.16. The plate is loaded at the top and the bottom boundary by a uniform stress σ. The fiber orientation is α. The material properties of the carbon/expoxy plate are shown in Table 5.6 [23].

Table 5.6 Material propteties of graphite/epoxy

Longitudinal Young's modulus, E_1	$329\ GPa$
Transverse Young's modulus, E_2	$6\ GPa$
Poisson's ratio, v_{12}	0.346
Shear modulus, G_{12}	$4.4\ GPa$
Mode I intralamina fracture energy for longitudinal loading, G_{10}	$15.49\ k\,J/m^2$
Mode I intralamina fracture energy for transver loading, G_{20}	$0.168\ k\,J/m^2$
Mass density, ρ	$1630\ kg/m^3$

Fig. 5.17, Fig. 5.18, Fig. 5.19, Fig. 5.20 and Fig. 5.21 show the peridynamic simulation results for $\alpha = 0°$, $\alpha = 30°$, $\alpha = 45°$, $\alpha = 60°$ and $\alpha = 90°$, respectively. In each figure, there are three contour plots with (a) vertical diaplacement of the plate, (b) strain energy density distribution and (c) local damge of the plate. Different color bars are associated with different plots with red indicating the highest value while blue the lowest value. Crack paths can be clearly seen from the strain energy density contour plot as there are always strain energy concentraions at the crack tips. The local damage is defined by Eqn. 2.12 and Enq. 2.13, which show different levels of damage. A proper cuttoff value can be defined to judge if there is a crack. In all cases, the crack propagates in the same direction as the fibers, which is consistent with the experimental observations from Wu [24]. The damage is due to the seperation between matrix and fiber. There is no fiber breakage.

As expected, in the $\alpha = 0°$ case, the crack propagates in the same direction as the pre-notch. This also matches with the computational and experimental results in Section 5.6. In the smaller angle case $\alpha = 30°$, aside from the major crack, which propagates in $30°$, there is matrix shattering at the sides of the plate in 0° direction. The matrix shattering happens before the crack starts to propagate as shown in Fig. 5.22. It starts at the lateral of the plate and propagates to the interior of the plate. From Fig. 5.18 (c), the matrix shattering is not as severe as the major crack since only 20% of the bonds are broken. However, in the major carck, more than 70% of the bonds are broken. This is why matrix shattering is only a material softening and may not be seen from experimental observation as reported in [24]. For the $\alpha = 90°$ case, the composite plate fails due to splitting caused by shear stress in the matrix. It which matches with the findings of Boger [25].

5.8 Conclusions

A peridynamic orthotropic material model baesd on the beam model is proposed in this chapter. There are four independent mateiral parameters in this model and it matches with the four material properties for two-dimensional orthotropic materials. The bond material properties depend on these four mateiral parameters and the angle between the bond orientation and fiber orientation. This results in the continuity of the bond stiffness function with no need of remeshing for different fiber orientations. This model is verified by a static tensile test and a vibration problem of a laminated beam.

Dynamic damage propagation problems in composite materials can br greatly benefited from peridynamics. The prediction of damage initiation and crack proagation of composite materials is complex using traditional methods, such as finite element analysis, due to its anisotropy. As investigated in peridynamic simulations, there is no need of tracking each crack propagation, finding different damage modes and applying different damage rules. Damage happes automatically. A single edge notch test is simulated in this chapter and the results match with the experimental results. Crack path and failure initiation of a center notch plate is predicted successfully by peridynamics when comparing with the experimental results.

References

[1] Dwivedi, S. K., Espinosa, Modeling dynamic crack propagation in fiber reinforced composites including frictional effects, Mechanics of Materials, **35**, 481-509 (2003)

[2] Xu, J., Askari, A., Wechner, O., Damage and Failure Analysis of Composite Laminates under Biaxial Loads, 48th AIAA/ASME/ASCE/AHS/ASC Structures, Structural Dynamics, and Materials Conference, April 23-26, 2007, Honolulu, Hawaii

[3] Hu, W., Ha, Y.D., Bobaru, F., Peridynamic model for dynamic fracture in unidirectional fiber-reinforced composites, Comput. Methods Appl. Mech. Engrg., 217-220 (2012)

[4] Silling, S. A., Reformulation of elasticity theory for discontinuities and long-range forces, J. Mech. Phys. Solids, **48**, 175-209 (2000)

[5] http://www.wolfram.com/mathematica/

[6] Daniel, I. M., Ishai, O., Engineering mechanics of composite materials, the Second Edition, Oxford University Press, Inc. (2006)

[7] Whitney, J. M., Structural Analysis Of Laminated Anisotropic Plates, Technomic Publishing Company, Inc. (1987)

[8] Lambros, J., Rosakis, J., Dynamic crack initiation and growth in thick unidirectional graphite/epoxy plates, Composite Science and Technology, **57**, 55-65 (1997)

[9] Zheng, S., Sun, C.T., A double-plate finite-element model for the impact-induced delamination problem, Composite Science and Technology, **53**, 111-118 (1995)

[10] Stout, M.G., Liu, C., Ellis, R.W., Haberman, K.S., Bennet, J.G., Williams, Addesio, F.L., Rosakis, A.J., Mechanics analysis and simulation of a graphite/epoxy composite plate, Experimental Mechanics, 187-192 (1998)

[11] Coker, D., Rosakis, A.J., Experimental observations of intersonic crack growth in asymmetrically loaded unidirectional composite plates, GALCIT-SM Reports 98-16. CALTECH, Pasadena, CA (1998)

[12] Coker, D., Rosakis, A.J., Experimental observations of intersonic crack growth in asymmetrically loaded unidirectional composite plates, Philosophical Magazine, **81**, 571-595 (2001)

[13] Huang, Y., Wang, W., Liu, C., Rosakis, A.J., Analysis of intersonic crack growth in unidirectional fiber-reinforced composites, Journal of the Mechanics and Physics of Solids, **47**, 1893-1916 (1999)

[14] Hwang, C., Geubelle, P., A spectral scheme to simulate dynamic fracture problems in composite, Computer Modeling in Engineering and Science, **4**, 45-56 (2000)

[15] Kumar, P., Kishore, N.N., Initiation and propagation toughness of delamination crack under an impact load, journal of the Mechanics and Physics of Solids, **46**, 1773-1787 (1998)

[16] Lo, C. Y., Nakamura T., Kushner, A.S., Dynamic failure analysis along interfaces in composite materials, Advanced Computational Methods for Material Modeling, AMD-vol.180, ASME, 115-124 (1993)

[17] Sun, C. T., Qian, W., The use of finite extension strain energy release rates in fracture of interfacial cracks, International Journal of Solids and Structures, **34**, 2595-2609 (1997)

[18] Pandey, R.K., Sun, C.T., Calculating strain energy release rate in cracked orthotropic beams, Journal of Thermoplastic Composite Materials, **9**, 381-395 (1996)

[19] Tippur, H.K., Krishnaswamy, S., Rosakis, A. J., Optical mapping of crack tip deformations using the method of transmission and reflection Coherent Gradient Sensing: A study of crack tip K-dominance, Int. J. Fract., **52**, 91-117 (1991)

[20] Tippur, H. V., Krishnaswamy, S., Rosakis, A. J., A coherent gradient sensor for crack tip measurements: Analysis and experimental results, Int. J. Fract., **48**, 193-204 (1991)

[21] Rosakis, A. J., Two optical techniques sensitive to gradients of optical path difference: The method of caustics and the coherent gradient sensor (CGS), Experimental Techniques in Fracture, J. Epstein, VCH, New York, 327-425 (1993)

[22] Donaldson, S. L., Fracture toughness testing of graphite/epoxy and graphite/PEEK composites, Composites, **16**, 103-112 (1985)

[23] Jose, S., Kumar, R. R., Jana, M. K., Venkateswara, R., Intralaminar fracture toughness of a cross –ply laminate and its constituent sub-laminates, Composites Science and Technology, 61, 1115-1122 (2001)

[24] Wu, E. M., Fracture mechanics of anisotropic plates, Composite material workshop, Lancaster, PA, Technomic Publishing Co. Inc, 20-43 (1968)

[25] Boger, P. B., Satyanarayana, A., Chunchu, P. B., Comparison of damage path prediction for composite laminates by explicit and standard finite element analysis tools, 47th AIAA/ASME/ASCE/AHS/ASC structures, structural dynamics, and materials conference, Newport, RI, May 1-4, 2006

[26] Satyanarayana, A., Bogert, P. B., Chunchu, P. B., The effect of delamination on damage path and failure load prediction for notched composite laminates, 48th AIAA/ASME/ASCE/AHS/ASC structures, structural dynamics, and materials conference, Honolulu, HI, April 23-26, 2007

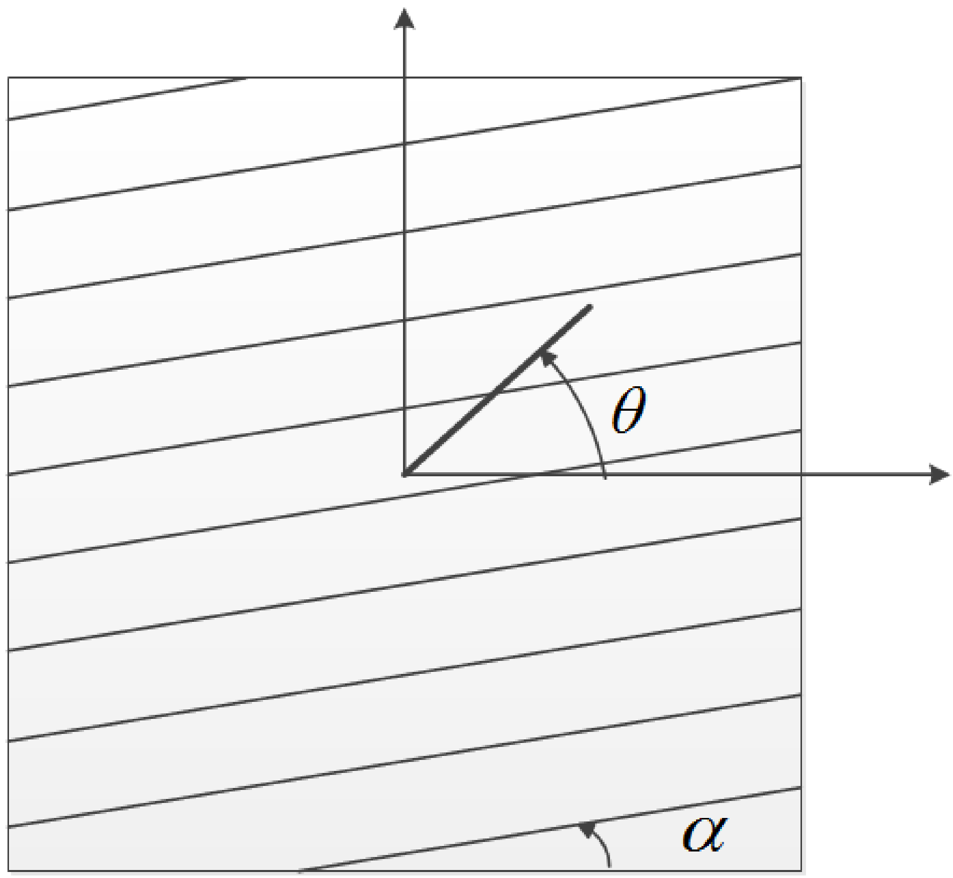

Figure 5.1 A composite plate with fiber in $\alpha°$ direction and a bond in $\theta°$ direction.

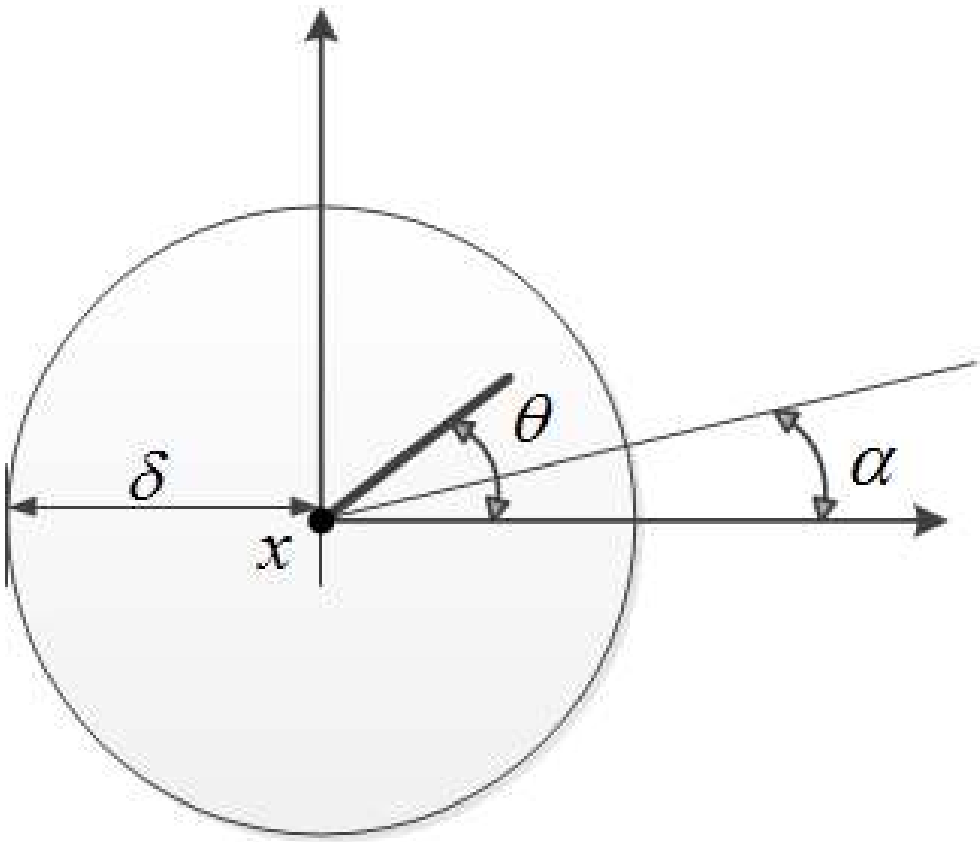

Figure 5.2 Coordinate system for calculating strain energy density at point x.

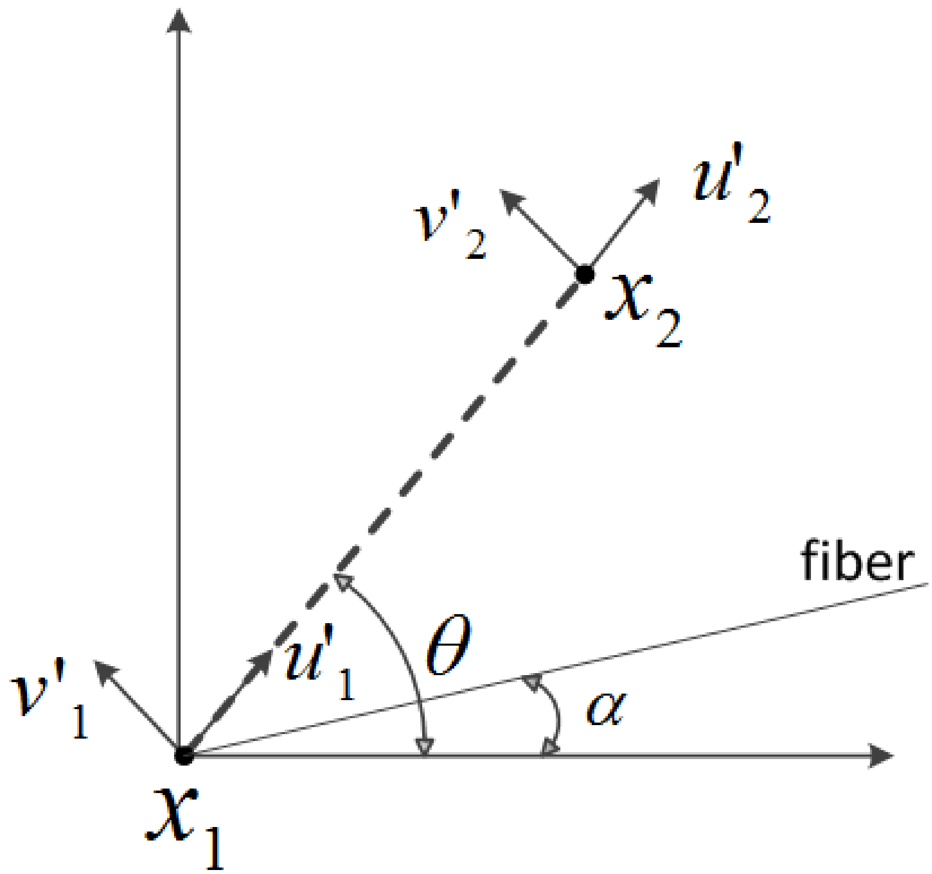

Figure 5.3 Beam model for orthotropic materials.

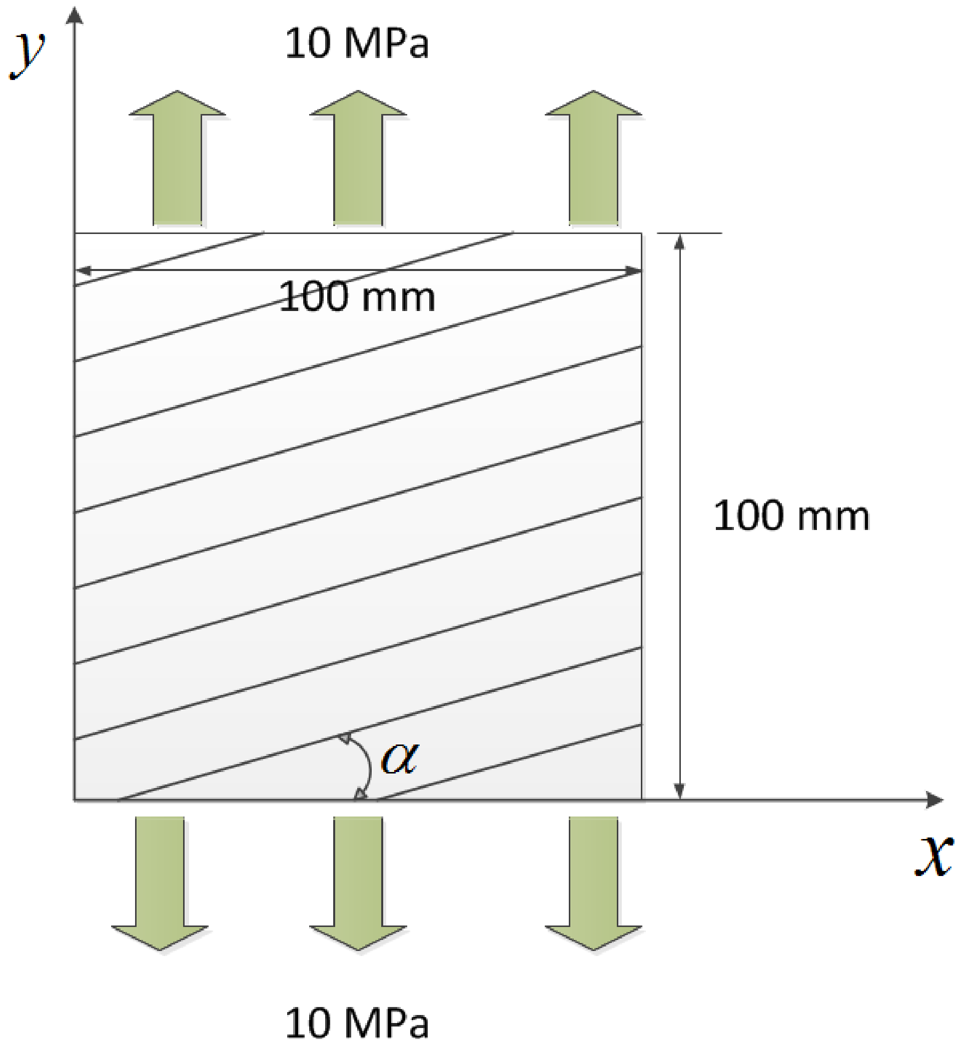

Figure 5.4 Pulling test in a composite laminate.

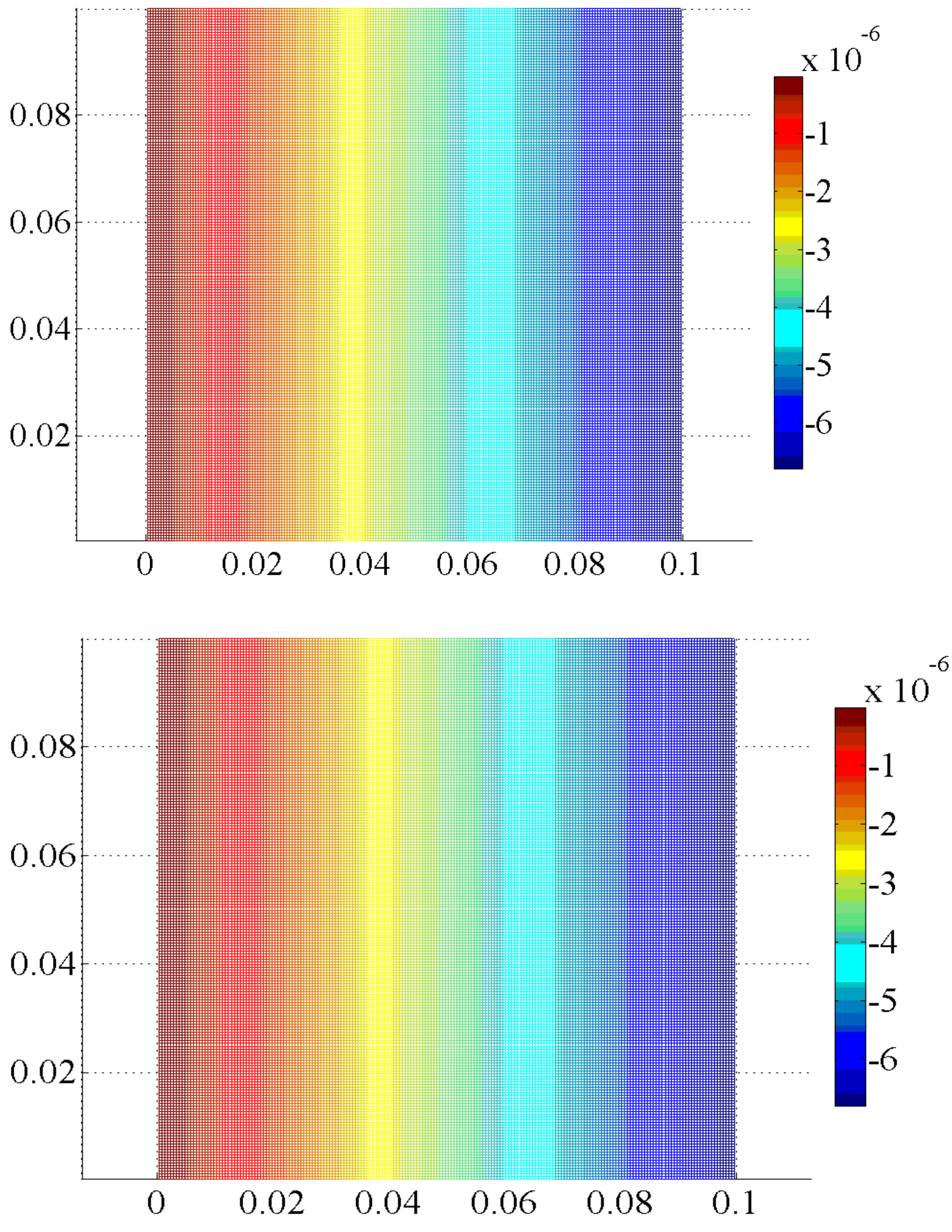

Figure 5.5 Comparison of u_x of 0° laminate calculated from peridynamics (top) and composite theory (bottom).

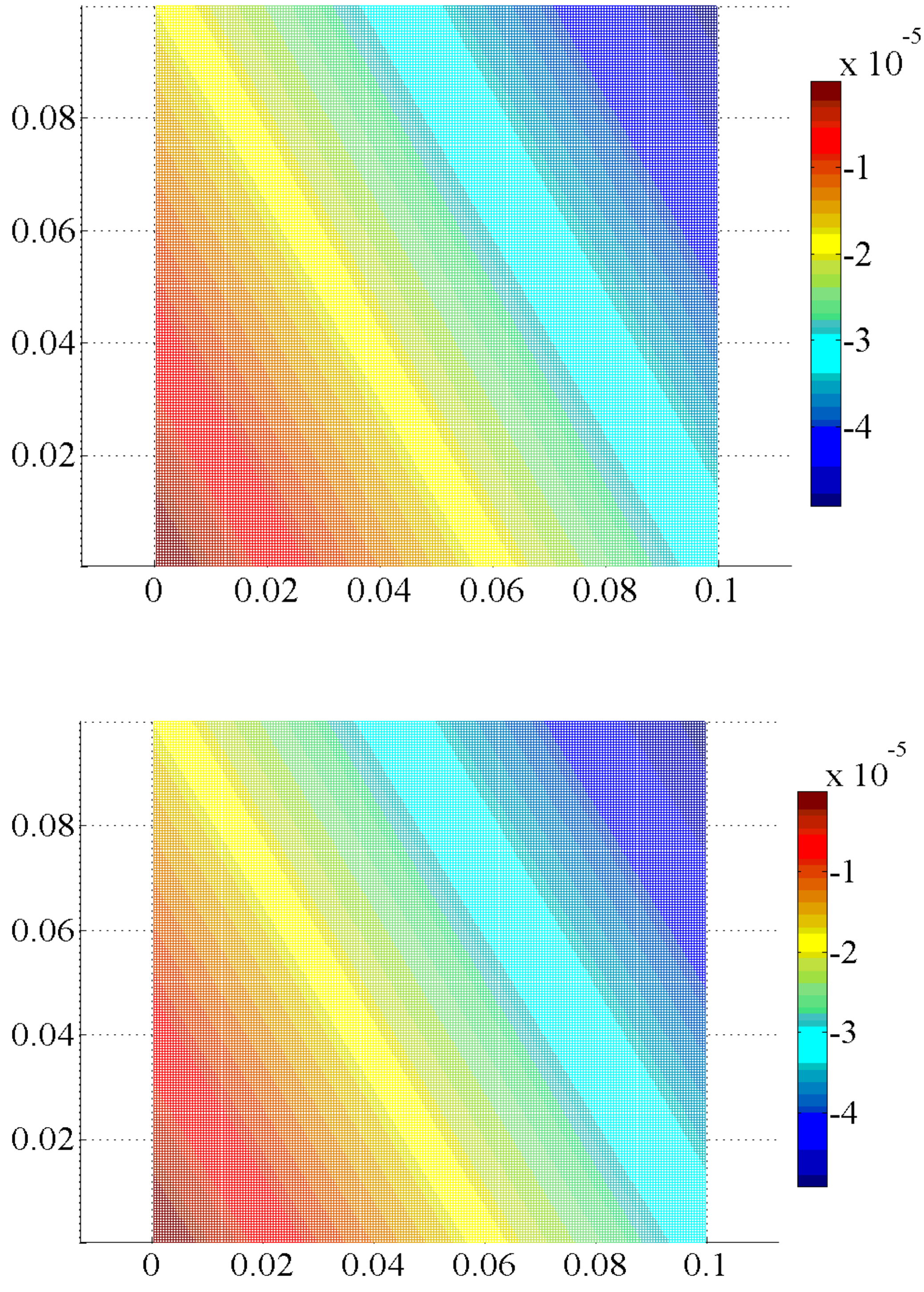

Figure 5.6 Comparison of u_x of 45° laminate calculated from peridynamics (top) and the composite theory (bottom).

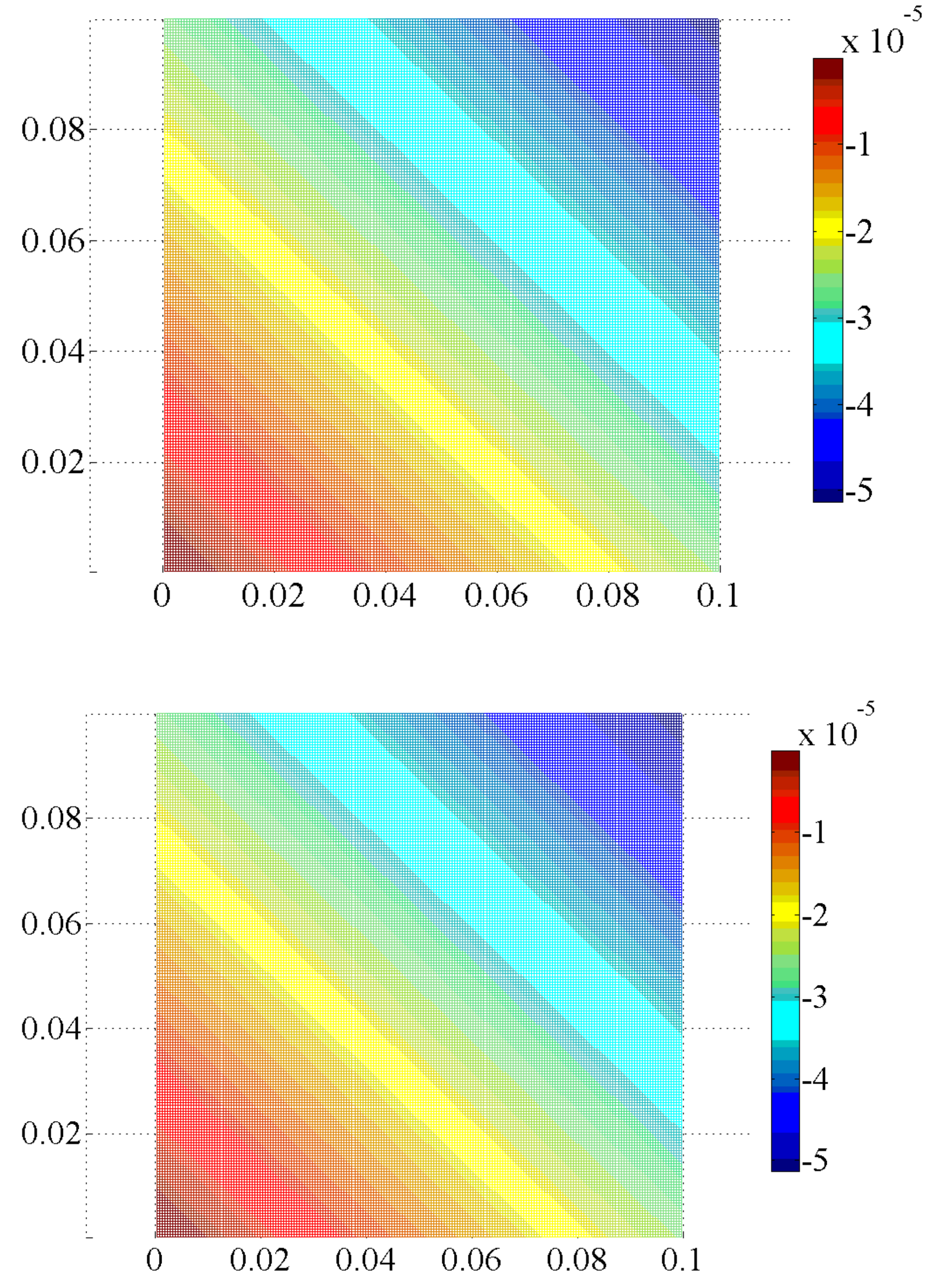

Figure 5.7 Comparison of u_x of 60° laminate calculated from peridynamics (top) and the composite theory (bottom).

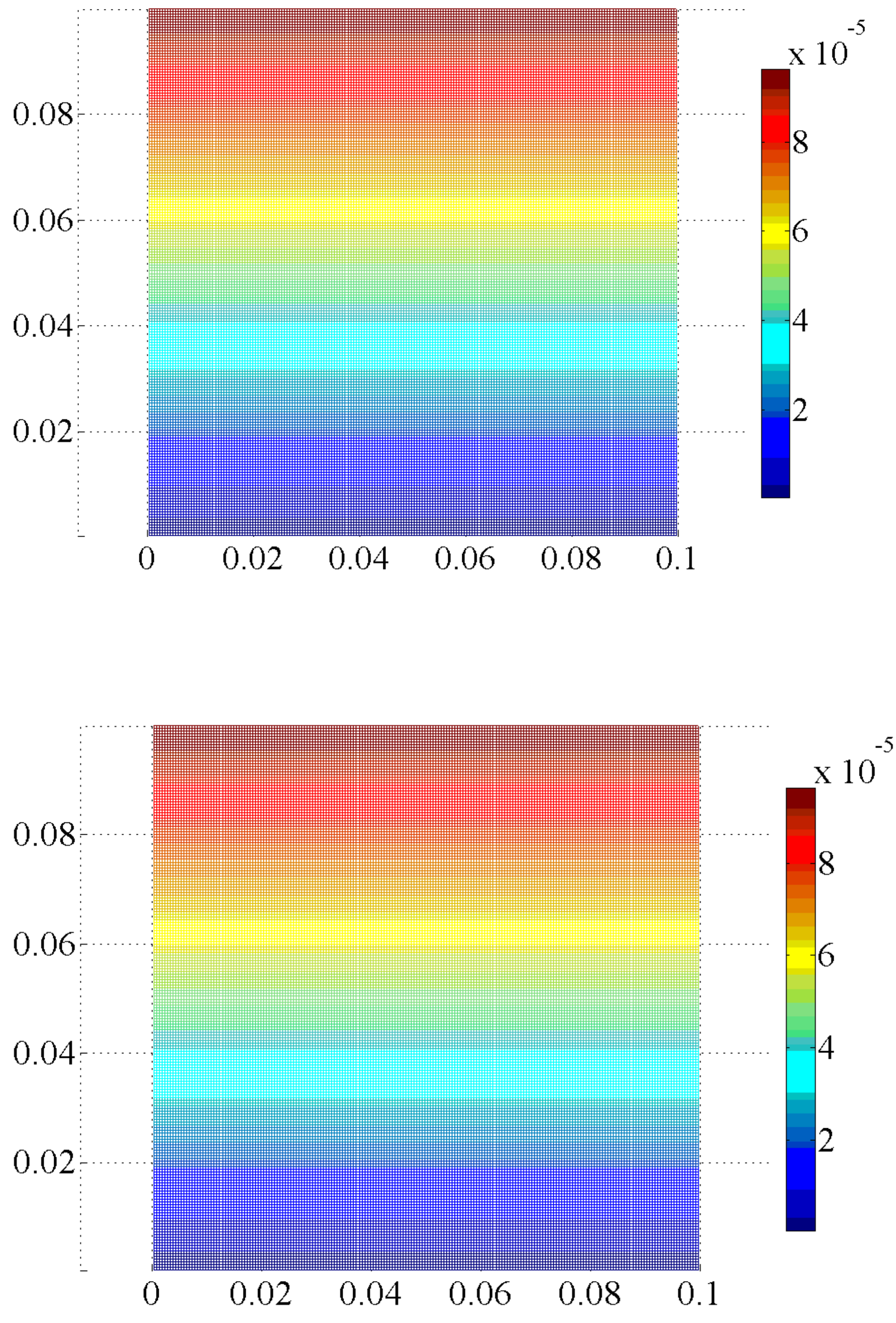

Figure 5.8 Comparison of u_y of 0° laminate calculated from peridynamics (top) and the composite theory (bottom).

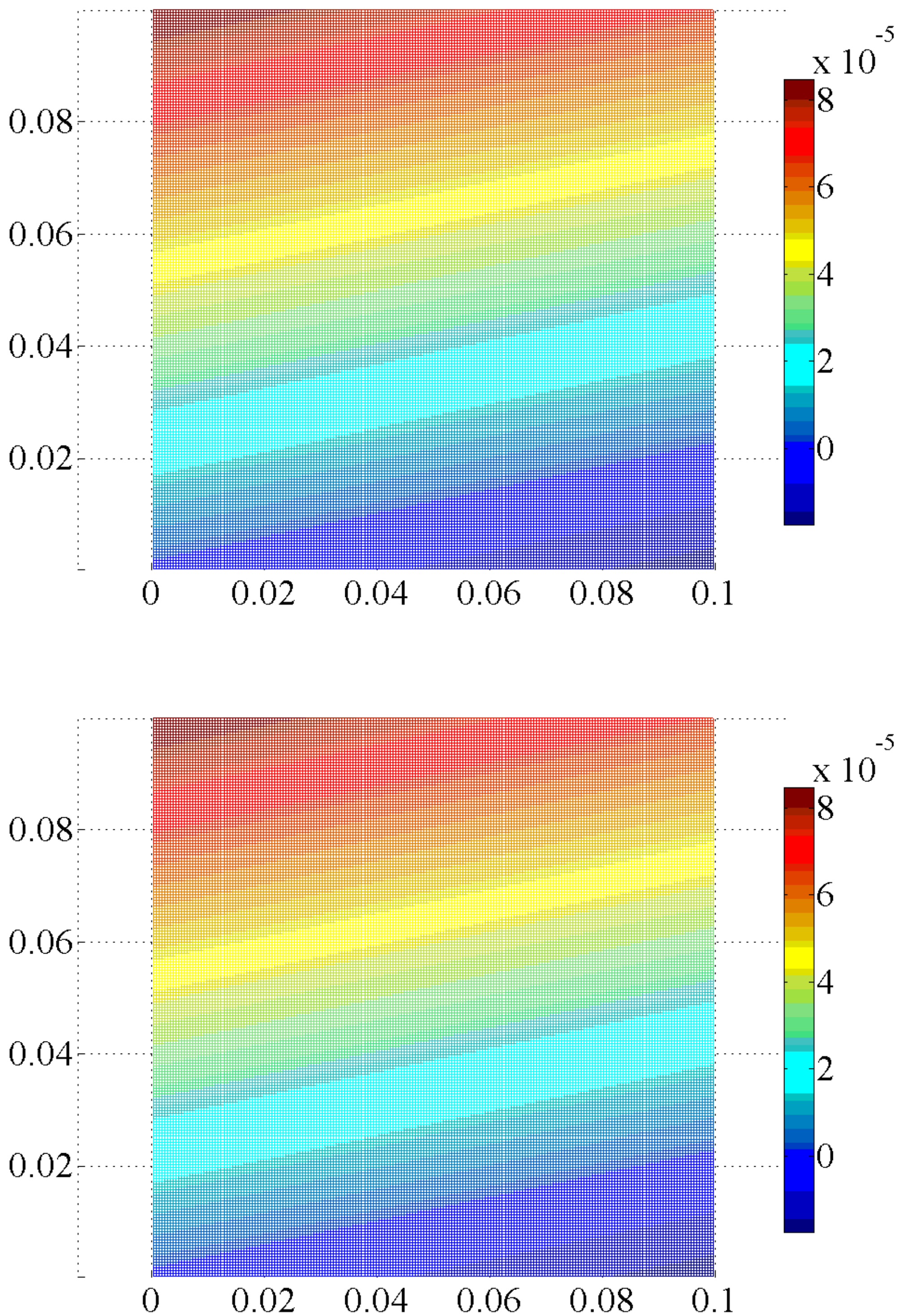

Figure 5.9 Comparison of u_y of 45° laminate calculated from peridynamics (top) and the composite theory (bottom).

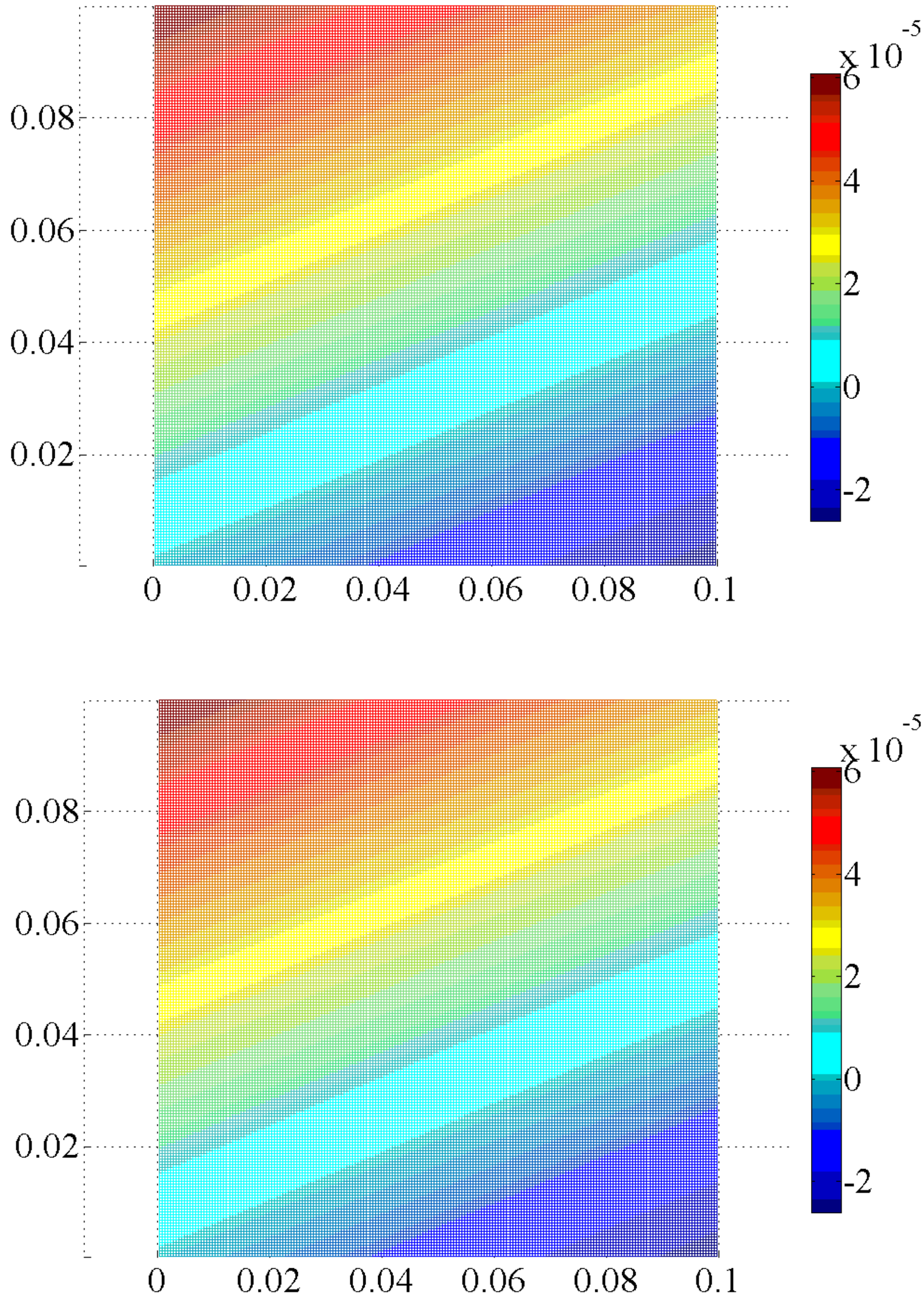

Figure 5.10 Comparison of u_y of 60° laminate calculated from peridynamics (top) and the composite theory (bottom).

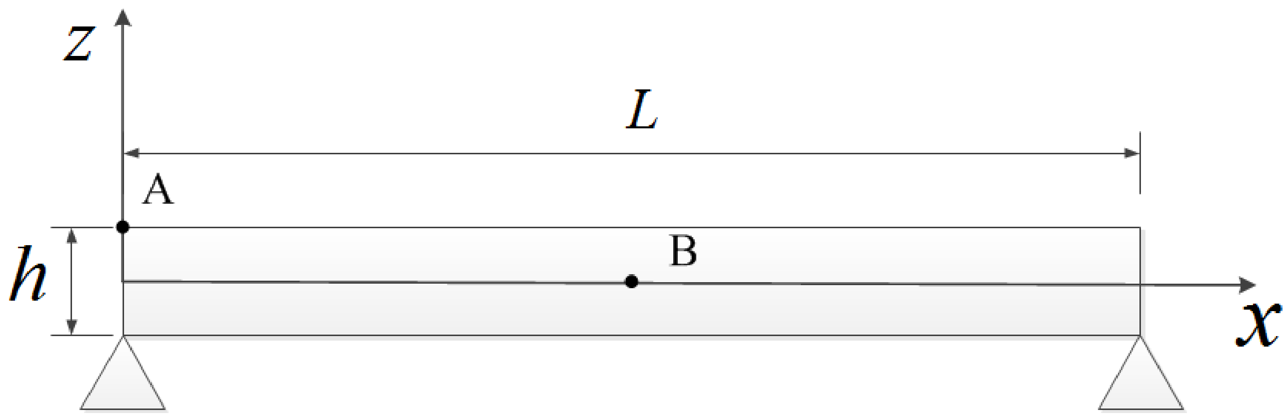

Figure 5.11 Free vibration of a laminated beam with fibers in x direction.

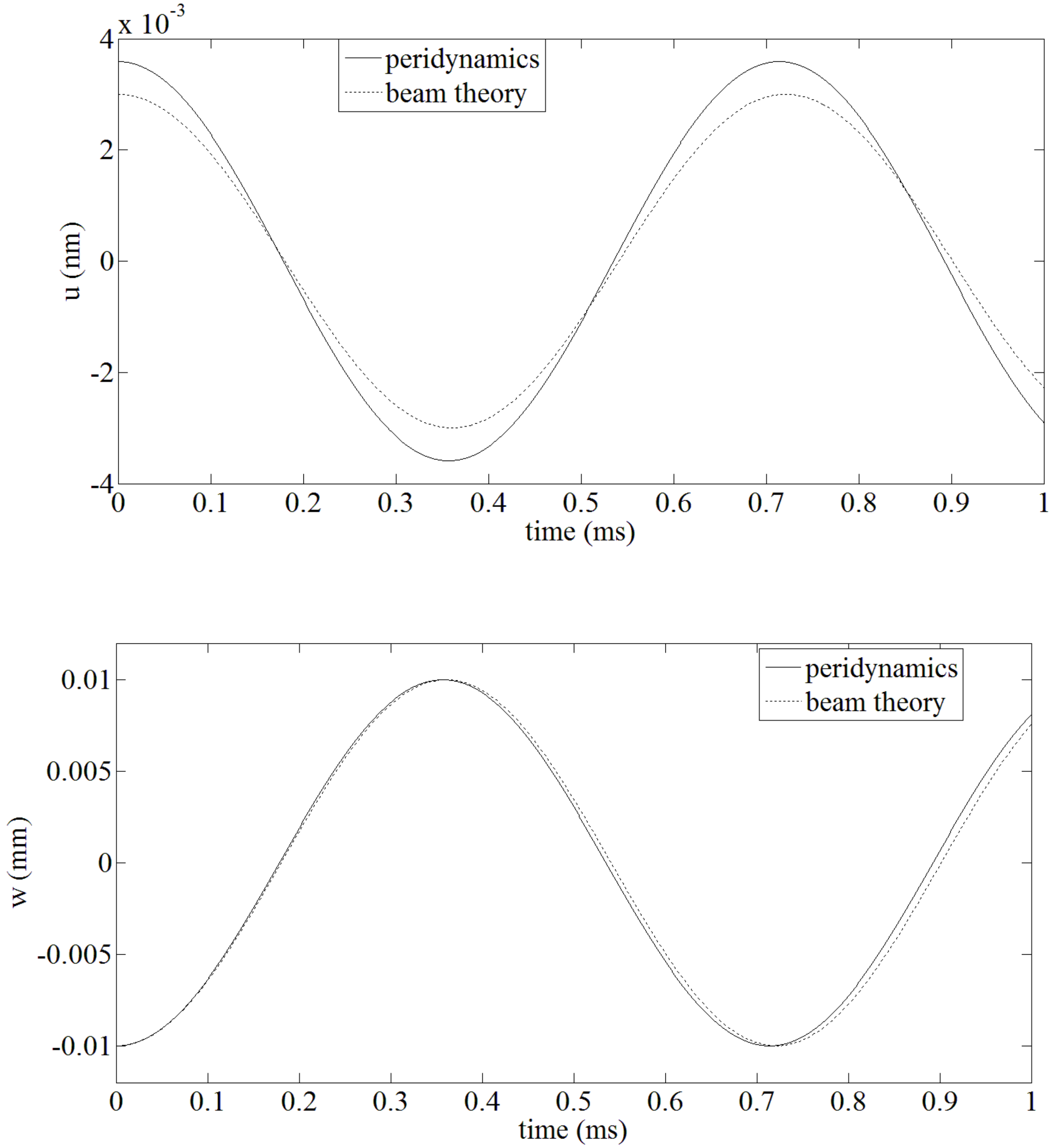

Figure 5.12 Peridynamic results compared with composite beam theory results with $\alpha = 5$.

Top: horizontal displacement u of point A. Bottom: vertical displacement w of point B.

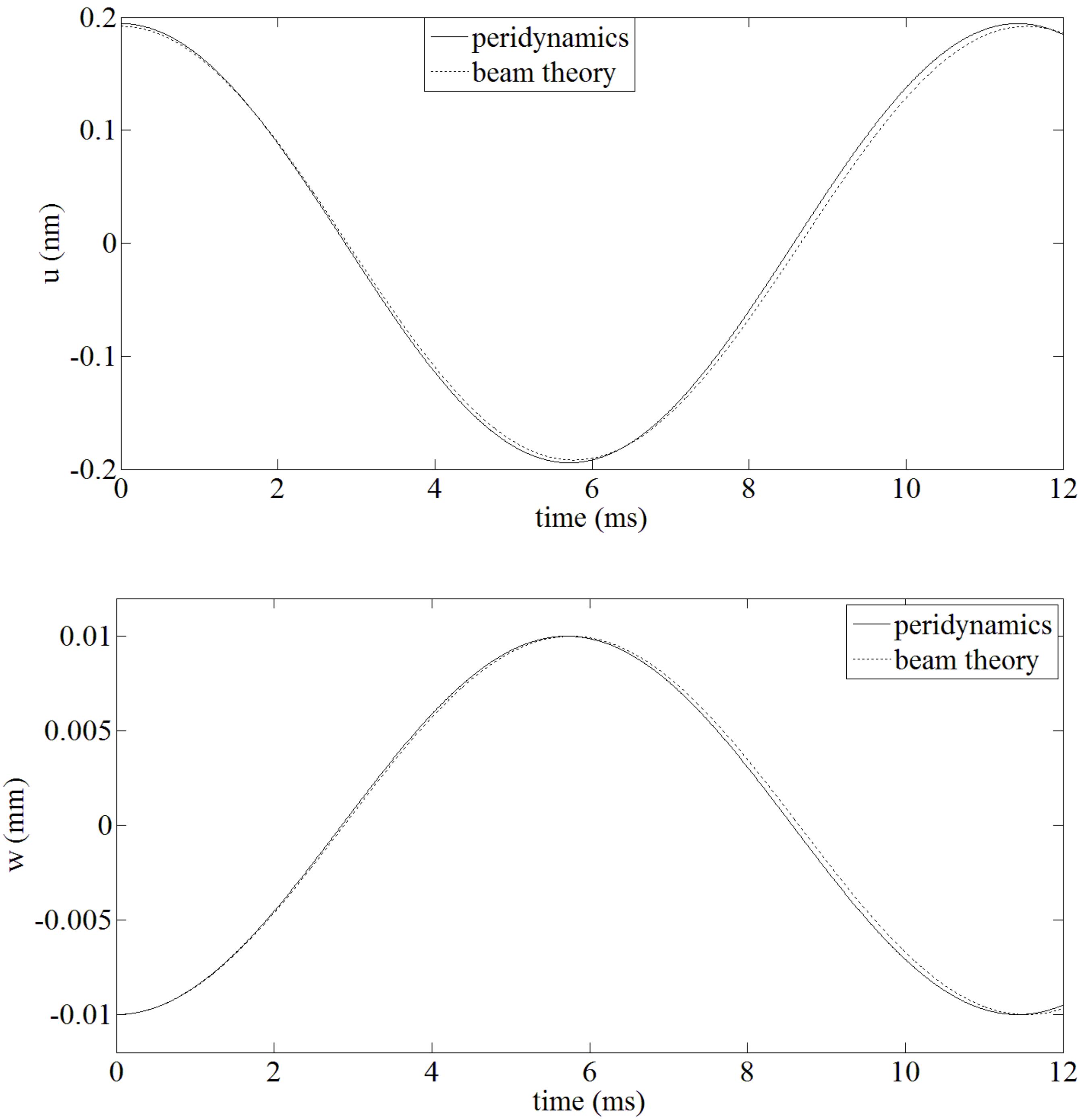

Figure 5.13 Peridynamic results compared with composite beam theory results with $a = 20$.

Top: horizontal displacement u of point A. Bottom: vertical displacement w of point B.

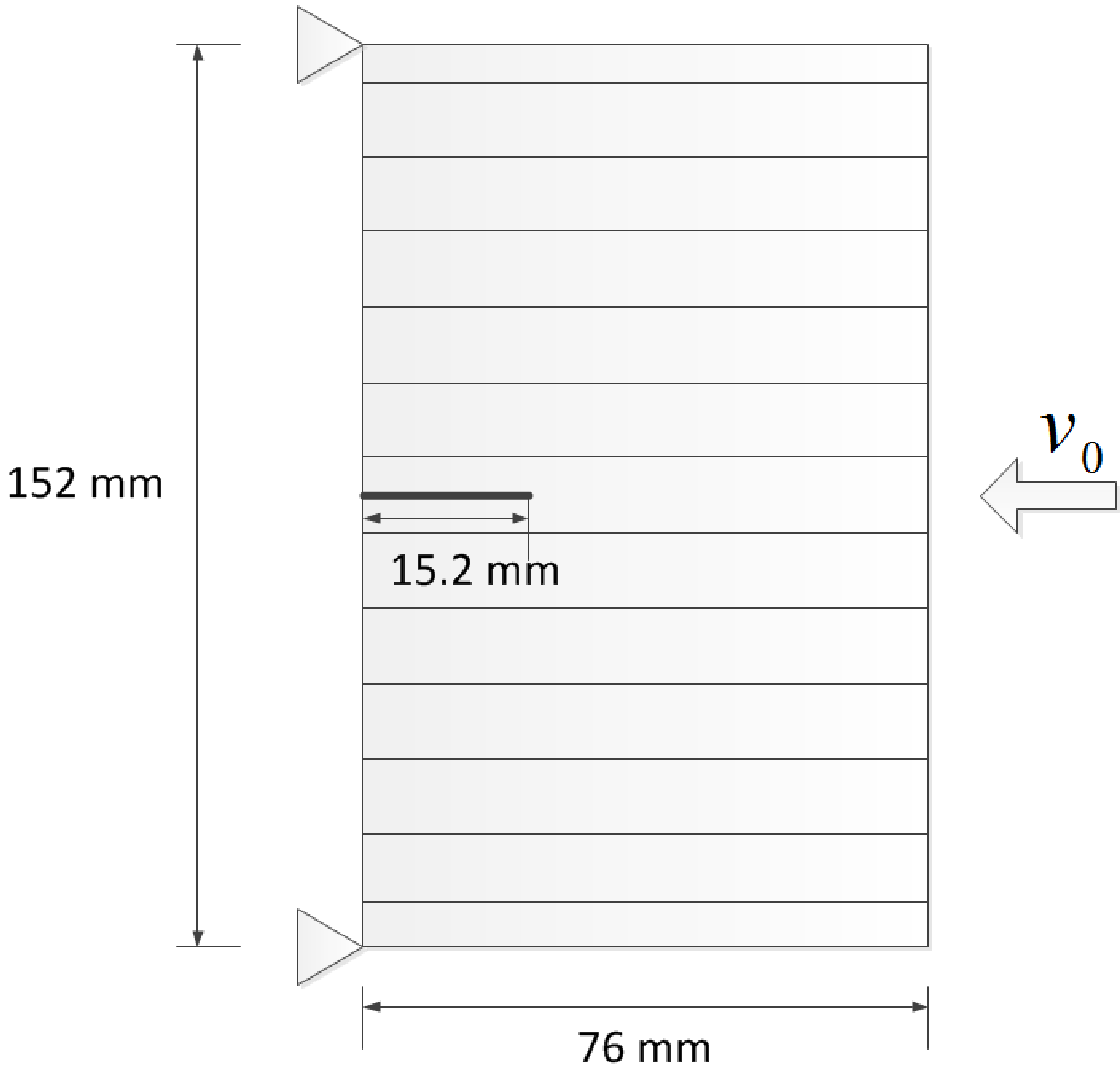

Figure 5.14 An unidirectional composite plate with single edge notch under three point bending.

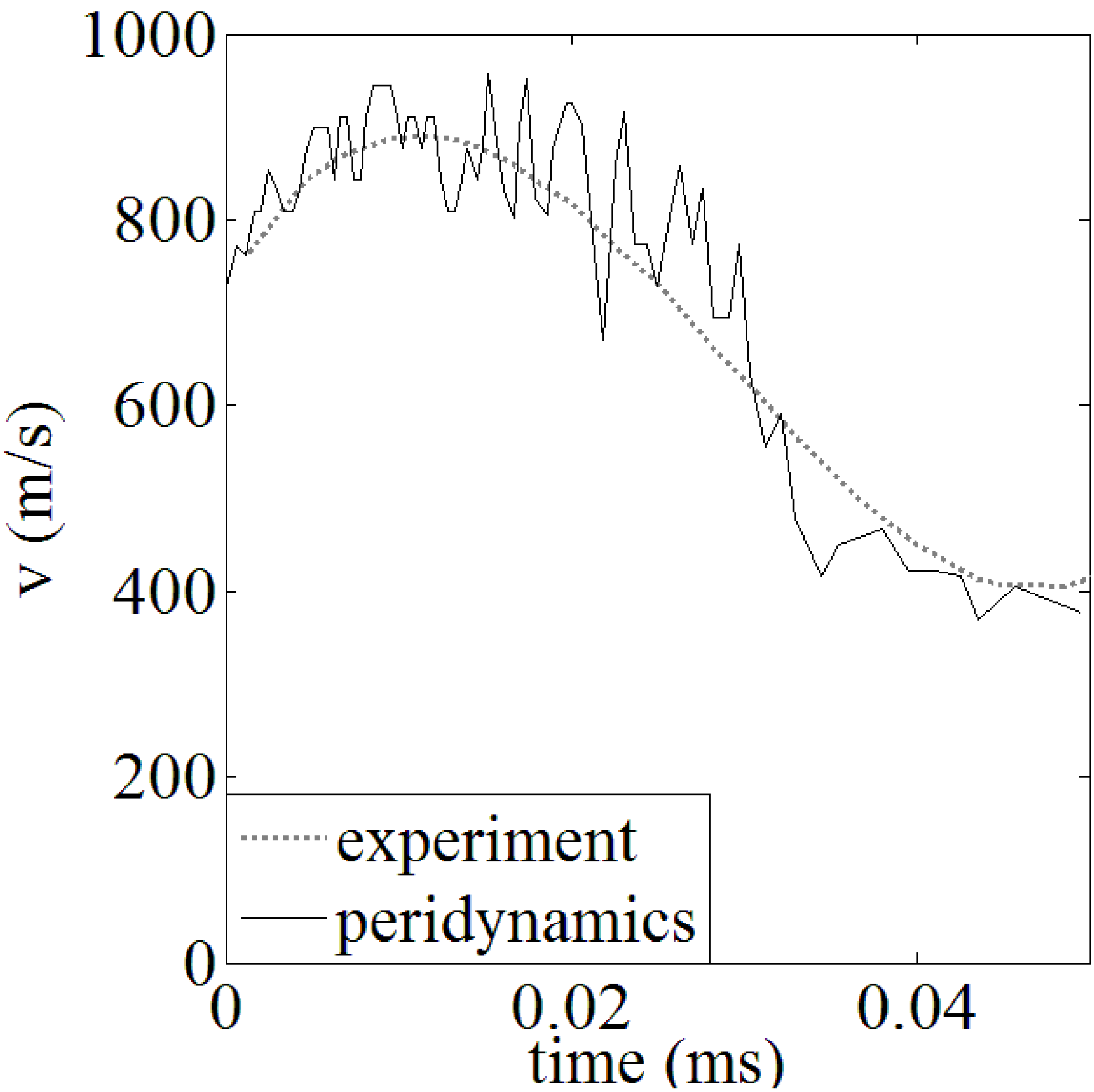

Figure 5.15 Comparison of crack propagation velocity between peridynamics and experiment.

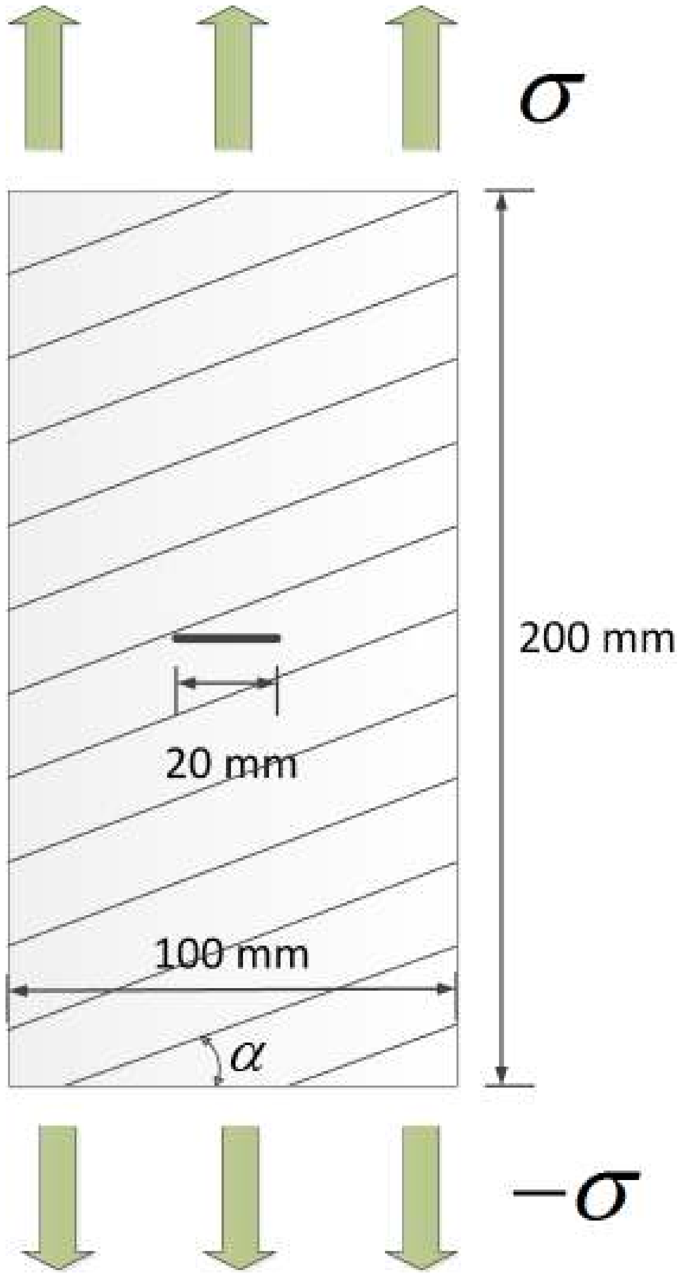

Figure 5.16 Compact tension test for a unidirectional composite plate.

(a)

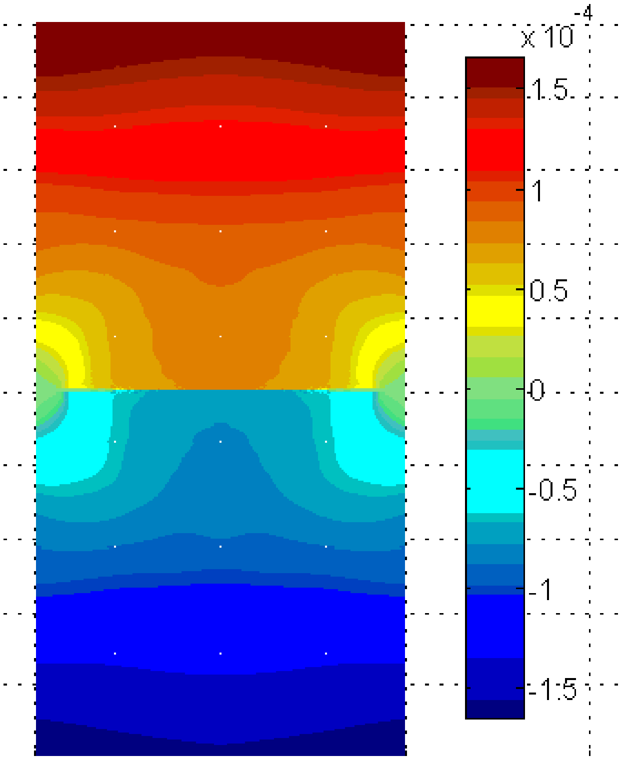

(b)

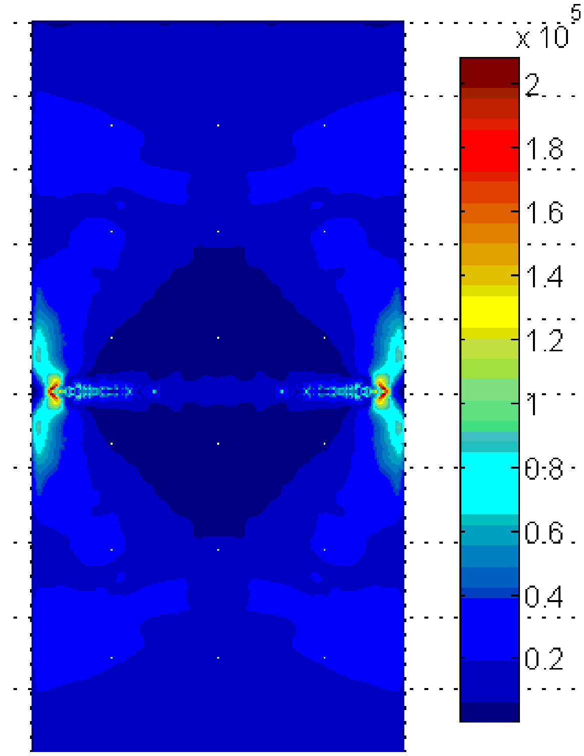

(c)

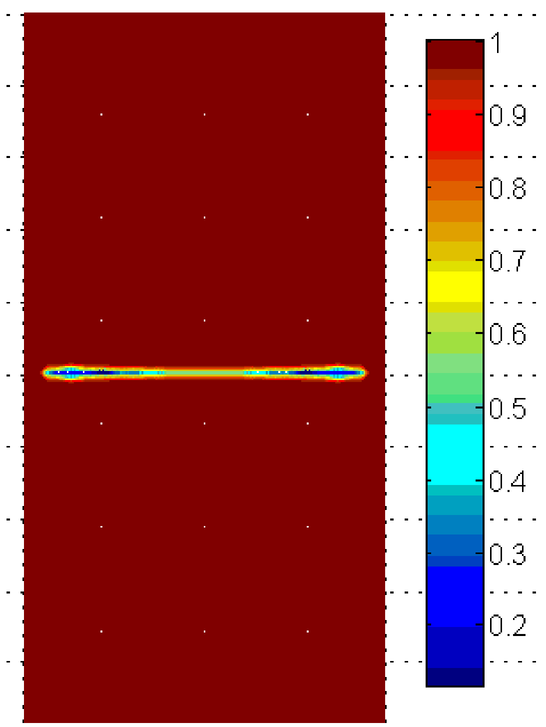

Figure 5.17 Simulation results for $t = 50\ \mu s$ and $\alpha = 0°$:

(a) vertical displacement, (b) strain energy density, (c) local damage.

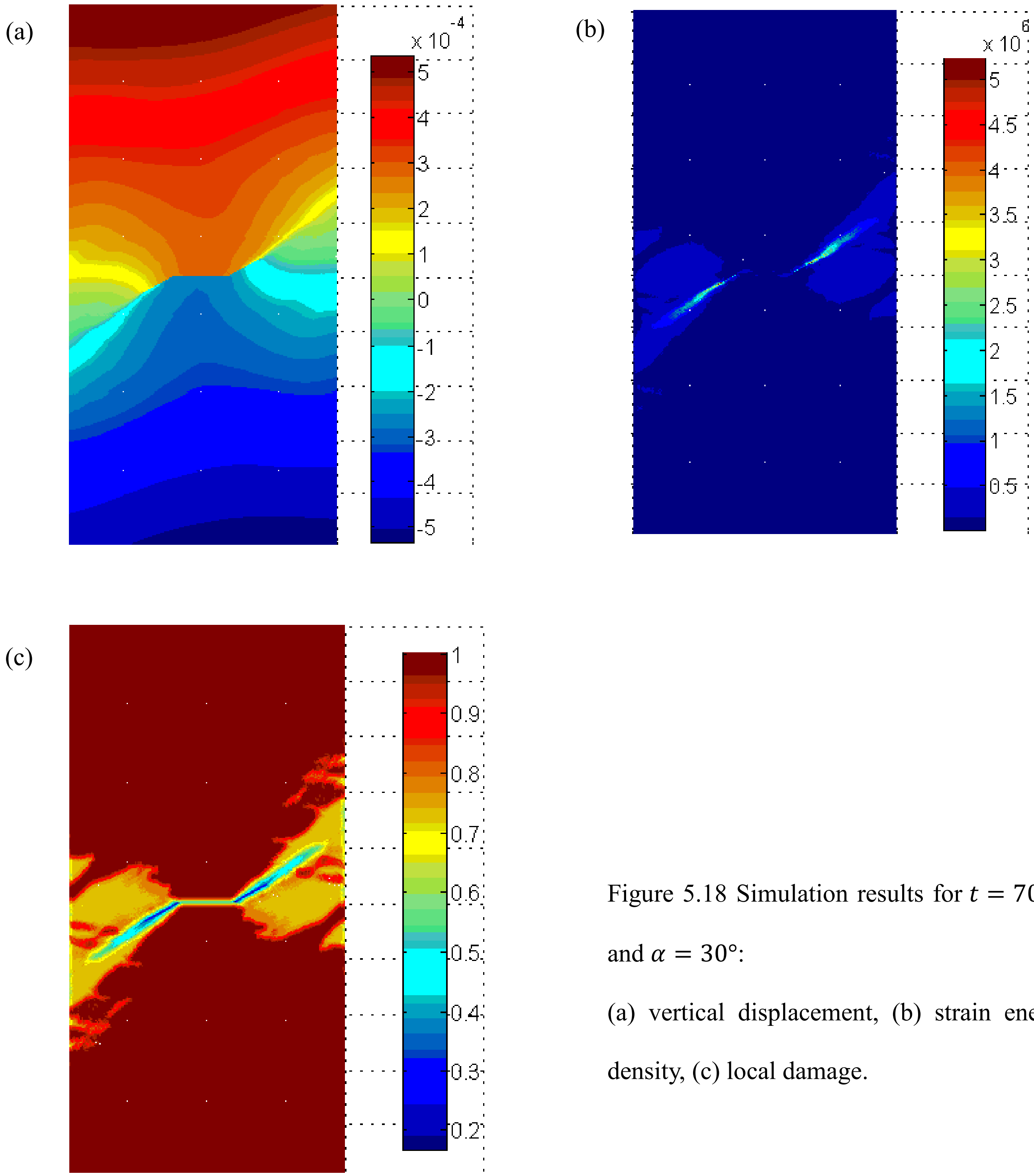

Figure 5.18 Simulation results for $t = 70\ \mu s$ and $\alpha = 30°$:

(a) vertical displacement, (b) strain energy density, (c) local damage.

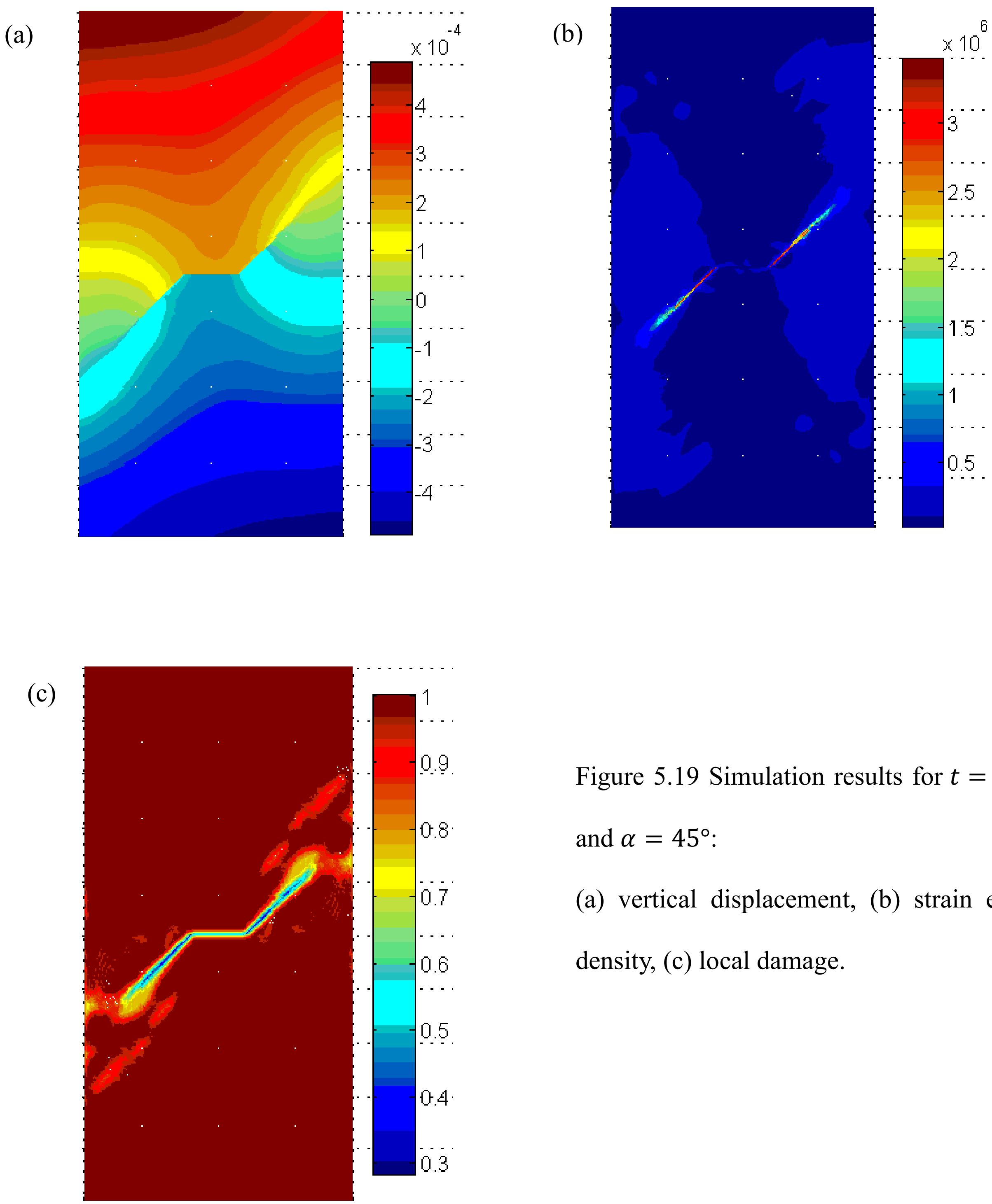

Figure 5.19 Simulation results for $t = 70\ \mu s$ and $\alpha = 45°$:

(a) vertical displacement, (b) strain energy density, (c) local damage.

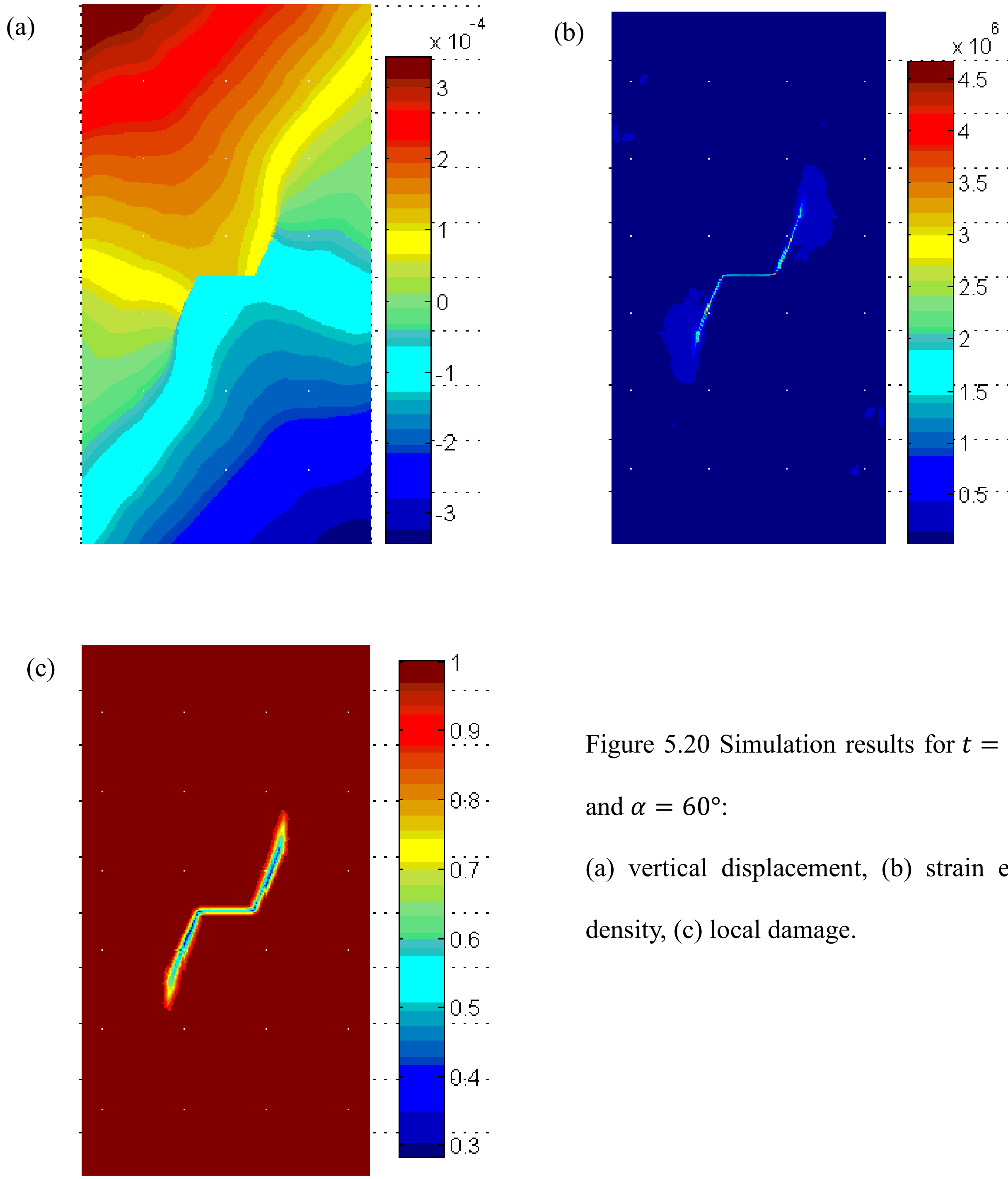

Figure 5.20 Simulation results for $t = 90\ \mu s$ and $\alpha = 60°$:

(a) vertical displacement, (b) strain energy density, (c) local damage.

(a)

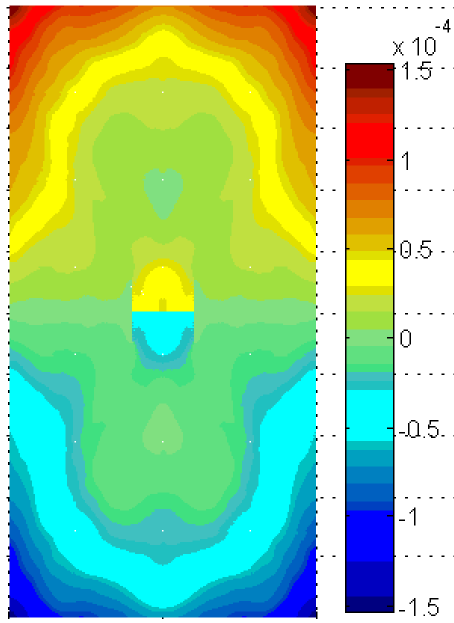

(b)

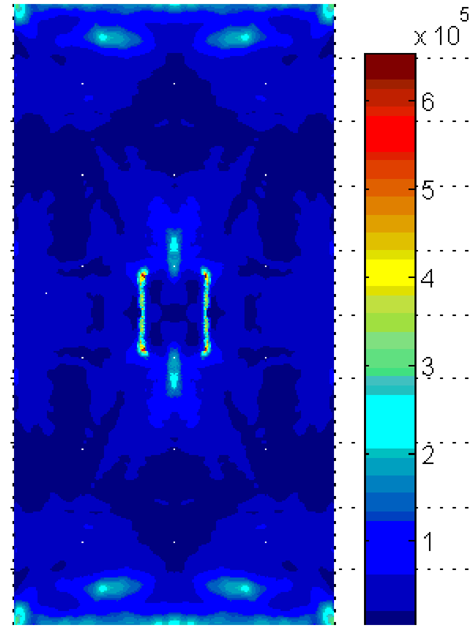

(c)

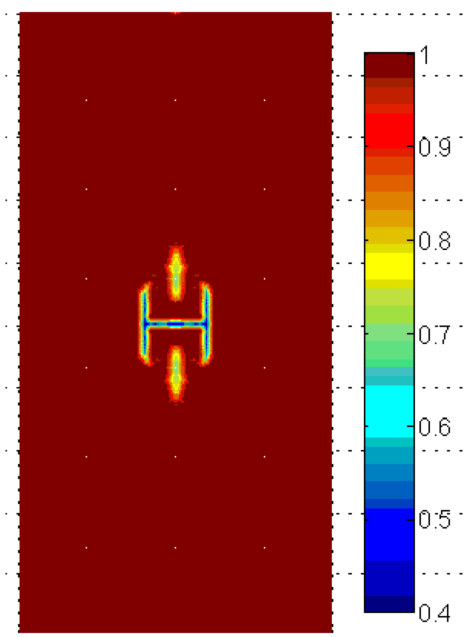

Figure 5.21 Simulation results for $t = 100.5\ \mu s$ and $\alpha = 90°$:

(a) vertical displacement, (b) strain energy density, (c) local damage.

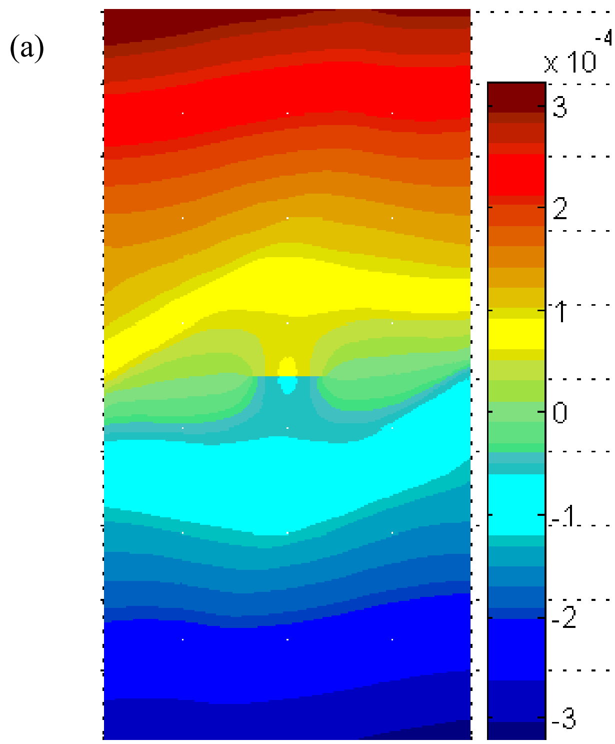

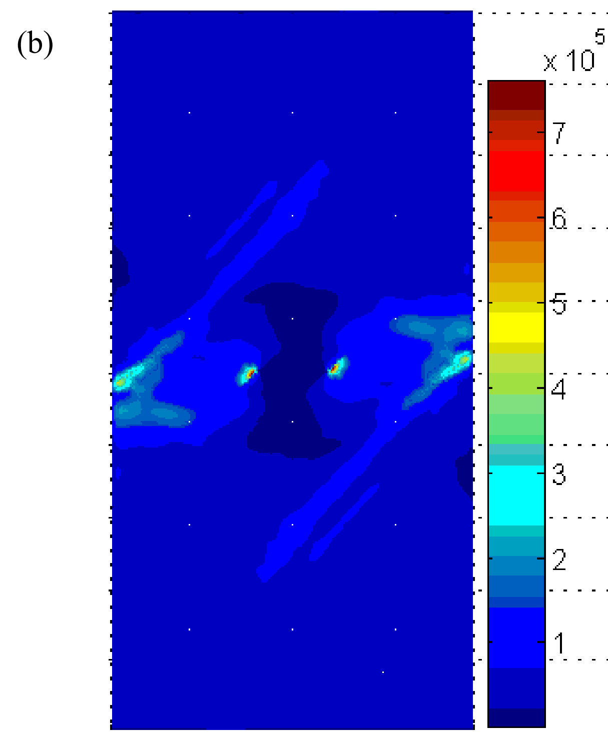

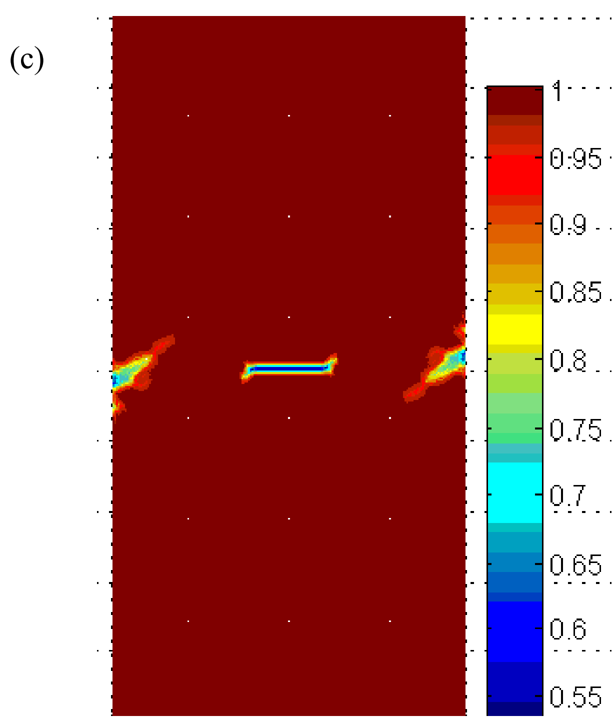

Figure 5.22 Simulation results for $t = 40\ \mu s$ and $\alpha = 30°$:

(a) vertical displacement, (b) strain energy density, (c) local damage.